

# Novel dual-photoelectrode photoelectrocatalytic system based on TiO<sub>2</sub> nanoneedle arrays photoanode and nitrogen-doped carbon dots/Co<sub>3</sub>O<sub>4</sub> photocathode for efficient water purification at low/no applied voltage

Zhongzheng Hu <sup>a,b</sup>, Minghua Zhou <sup>a,b,\*</sup>, Hubdar Ali Maitlo <sup>a,b</sup>, Ruiheng Liang <sup>a,b</sup>, Yang Zheng <sup>a,b</sup>, Huizhong Wu <sup>a,b</sup>, XiangRu Song <sup>a,b</sup>, Omotayo A. Arotiba <sup>c,d</sup>

<sup>a</sup> Tianjin Key Laboratory of Environmental Technology for Complex Trans-Media Pollution, College of Environmental Science and Engineering, Nankai University, Tianjin 300350, China

<sup>b</sup> Tianjin Advanced Water Treatment Technology International Joint Research Center, College of Environmental Science and Engineering, Nankai University, Tianjin 300350, China

<sup>c</sup> Department of Chemical Sciences, University of Johannesburg, Doornfontein 2028, South Africa

<sup>d</sup> Centre for Nanomaterials Science Research, University of Johannesburg, South Africa



## ARTICLE INFO

**Keywords:**  
Photoelectrocatalysis  
Dual-photoelectrode  
Mechanism  
Low applied voltage  
Water Purification

## ABSTRACT

A novel tandem photoelectrocatalysis (PEC) cell consisting of TiO<sub>2</sub> nanoneedle arrays (TiO<sub>2</sub> NNs/Ti mesh) photoanode and nitrogen-doped carbon dots (NCDs) modified Co<sub>3</sub>O<sub>4</sub> photocathode (NCDs/Co<sub>3</sub>O<sub>4</sub>/Ti mesh) is designed to work at low/no applied voltage. Electrochemical impedance spectroscopy, incident photo-to-current conversion efficiency, and open-circuit voltage confirmed enhancement in the photogenerated charge transfer efficiency and internal photovoltage, which is due to synergistic effect in combination of two photoelectrodes. Under light-emitting diode (LED) light irradiation and cell voltage of 0.4 V, the system represented high activity and stability (0.0527 min<sup>-1</sup> after 20 cycles) and energy efficiency (2.09 kWh m<sup>-3</sup> order<sup>-1</sup>) for sulfadiazine removal. Based on the main •OH-induced reaction, the cooperative operation mechanism of TiO<sub>2</sub> NNs/Ti mesh and NCDs/Co<sub>3</sub>O<sub>4</sub>/Ti mesh for sulfadiazine degradation was elaborated. Finally, the high performance under real water matrices or real sunlight irradiation without external voltage confirmed the feasibility of this PEC system in practical application for efficient water purification.

## 1. Introduction

The presence of emerging organic water pollutants (such as antibiotics, phenolic compounds, and dyes) has significantly been increased with rapid population growth and industrialization [1–3]. Among them, sulfadiazine (SDZ) is widely served as veterinary medicine, whose occurrence in the surface water was reported to be reached 0.17 mg L<sup>-1</sup> [4]. Due to the potential long half-life of SDZ, it may alter microbial communities and affect ecological diversity, thus threatening ecological environment security and human health [5–7]. It has been reported that the removal efficiency of SDZ in wastewater treatment plants (WWTP) by activated sludge process was low (48–77%), making the WWTP effluents one of the main sources of SDZ in the aquatic environment [3]. As is known, an effectual wastewater treatment and reuse is important

and inevitable option to cope up with contaminated water [8]. Therefore, it is presumed that the development of an efficient, low-cost, and eco-friendly wastewater treatment technology for pollutant (e.g. SDZ) removal is highly desired.

Solar energy is a free, green and renewable energy source that is ubiquitously distributed all over the world with 36000 TW per year on land [9]. Thus, photoelectrocatalysis (PEC) technology poses great prospect in environmental remediation due to in-situ production of reactive oxygen species (ROS) via utilizing solar energy [10]. However, some challenges are still needed to be solved to make the PEC system a practically applicable option for organic pollutant abatement. Firstly, the single-photoelectrode PEC system is usually energy-expensive, which requires a higher external bias potential (1.0–2.0 V vs. Ag/AgCl) for efficient removal of organic pollutants [11–16]. Besides,

\* Corresponding author at: Tianjin Key Laboratory of Environmental Technology for Complex Trans-Media Pollution, College of Environmental Science and Engineering, Nankai University, Tianjin 300350, China.

E-mail address: [zhoumh@nankai.edu.cn](mailto:zhoumh@nankai.edu.cn) (M. Zhou).

photoanode or photocathode materials have been shown to be unstable because of corrosion or strong potential dependency, especially when the quasi-Fermi energy levels of the photoinduced electrons/holes are more negative/positive than the thermodynamic reduction/oxidation potential of the photocatalyst [17,18]. For example, Cu<sub>2</sub>O can be converted to CuO and Cu through self-redox reaction under continuous irradiation [19].

To lower energy demand, the dual-photoelectrode PEC cell connected with photoanode and photocathode has been developed [20]. A dual-photoelectrode PEC system includes two light absorbers, a photoanode and a photocathode, where the quasi-Fermi level difference between the photoelectrodes will form an internal photovoltage [21]. The sizable photovoltage can offset part or even all of input electrical energy required for the reaction [22]. To date, TiO<sub>2</sub> as an n-type semiconductor with some promising properties (e.g., stability, nontoxicity, low price, and suitable quasi-Fermi energy position) has been extensively used as an effective photoanode for pollutant removal [12]. Despite the made progress, recent works suggest that the catalytic activity of TiO<sub>2</sub> catalysts with one-dimensional (1D) nanostructures on plate-like substrates is limited for contaminant degradation [16,23]. Consequently, a three-dimensional (3D) branched array structure was developed consisting of 1D nanorods/nanowires grown on an interconnected 3D network structure [13,24]. Such an architecture exhibits higher performance due to the excellent charge transport, fast mass transport, and efficient light harvesting. Therefore, TiO<sub>2</sub> with a branched 3D array structure can be a promising photoanode. The photocathode plays a crucial role in the design of a high-efficiency and energy-saving dual-photoelectrode PEC system. Co<sub>3</sub>O<sub>4</sub>, a p-type semiconductor, can be effectively activated by visible light due to the appropriate bandgap (Eg ~ 2.3 eV) [25]. It has been reported that the quasi-Fermi level of p-type semiconductor matches well with n-type semiconductor [20], thus it would be feasible to use Co<sub>3</sub>O<sub>4</sub> as a photocathode and TiO<sub>2</sub> as a photoanode in a dual-photoelectrode PEC system. However, the higher photoinduced carries recombination rates and the biologically toxic cobalt ion limit the extensive application of pure Co<sub>3</sub>O<sub>4</sub> as a photocathode [26,27]. To address these shortcomings in pure Co<sub>3</sub>O<sub>4</sub>, introducing cocatalyst is one of the possible strategies. Nitrogen-doped carbon dots (NCDs) are emerging cocatalysts due to their promising properties including high chemical stability, cost-effectiveness, low intrinsic toxicity, and good electron reservoir properties [23,28]. Meanwhile, there are reports on the electron sink effect of NCDs, which can extract more electrons and effectively hinder the electron-hole recombination [29]. Hence, coupling NCDs with Co<sub>3</sub>O<sub>4</sub> to form NCDs/Co<sub>3</sub>O<sub>4</sub> heterojunction is an effective strategy to improve the separation rate of electron-hole pairs and enhance the stability of photocathode.

Considering these characteristics, here we have selected a 3D interconnected Ti mesh as a substrate for developing a photoelectrode to improve mass transfer. The TiO<sub>2</sub>/Ti mesh nanoneedle arrays (TiO<sub>2</sub> NNs/Ti mesh) photoanode and the novel nitrogen-doped carbon dots/Co<sub>3</sub>O<sub>4</sub> nanoneedle arrays heterojunction (NCDs/Co<sub>3</sub>O<sub>4</sub>/Ti mesh) photocathode were prepared by a simple hydrothermal method and annealing treatment. The dual-photoelectrode PEC systems using TiO<sub>2</sub> NNs/Ti mesh photoanode and NCDs/Co<sub>3</sub>O<sub>4</sub>/Ti mesh photocathode was developed for the first time, which could degrade pollutant under low/no external voltage condition. Relatively, this advanced dual-photoelectrode PEC system possessed superior activity and energy efficiency for organic contaminants compare to a single-photoelectrode PEC system. Moreover, trapping experiments, electron paramagnetic resonance (EPR) tests, and •OH quantitative analysis were carried out to identify the role of ROS in this PEC system. Finally, the practical application prospects (e.g., photoelectrocatalytic performance, environmental adaptability, energy consumption, and long-term stability) of this PEC system were evaluated to justify it as an option for treatment of real wastewater containing organic contaminants.

## 2. Materials and methods

### 2.1. Photoelectrodes preparation

In order to remove grease and dirt, Ti mesh (surface area of 2.8 × 4 cm<sup>2</sup> and wire diameters of 0.1 mm) was first sonicated in acetone (≥ 99.5%) for 30 min, then in ethanol (≥ 99.7%) for 30 min, and finally in deionized water (DW) for 30 min. A previously reported synthesis method was used to develop the TiO<sub>2</sub> NNs/Ti mesh photoanode [11].

The details of the NCDs synthesis method are given in the [supporting information](#). The NCDs/Co<sub>3</sub>O<sub>4</sub>/Ti mesh photocathode was prepared by a hydrothermal method and annealing treatment. (Fig. 1a). Typically, 2.9 mmol Co(NO<sub>3</sub>)<sub>2</sub>•6 H<sub>2</sub>O, 5.7 mmol NH<sub>4</sub>F, and 14.3 mmol CO(NH<sub>2</sub>)<sub>2</sub> were dissolved together in deionized water to form a homogeneous solution. The 0.50 g L<sup>-1</sup> NCDs were gradually added to the above solution under 30 min stirring. Afterwards, this solution along with the pretreated Ti mesh was transferred to a 50 mL Teflon-lined autoclave, and heated at 120 °C for 5 h. Subsequently, the sample was calcined at 350 °C (ramping rate: 5 °C min<sup>-1</sup>) for 2 h to obtain the 3D structured 0.50-NCDs/Co<sub>3</sub>O<sub>4</sub>/Ti mesh photocathode. Similar synthesis procedure was used to prepared 0.25-NCDs/Co<sub>3</sub>O<sub>4</sub>/Ti mesh and 1.00-NCDs/Co<sub>3</sub>O<sub>4</sub>/Ti mesh with the addition of 0.25 g L<sup>-1</sup> and 1.00 g L<sup>-1</sup> NCDs. Without explanation, NCDs/Co<sub>3</sub>O<sub>4</sub>/Ti mesh was used to represent 0.50-NCDs/Co<sub>3</sub>O<sub>4</sub>/Ti mesh in this work.

### 2.2. Characterizations

The morphology and crystal structures of the prepared photoelectrodes were investigated by field-emission scanning electron microscopy (FESEM, LEO-1530VP) equipped with the energy-dispersive X-ray spectroscopy (EDS), and X-ray diffraction (XRD, Philips-12045 B/3 diffractometer with Cu-Kα irradiation). The X-ray photoelectron spectra (XPS) and ultraviolet photoelectron spectroscopy measurements were conducted on the Thermo Scientific ESCALAB 250Xi with a monochromatic Al- Kα source or He-I α source ( $h\nu = 21.22$  eV), respectively. The UV-vis diffuse reflectance spectra (UV-vis DRS) was collected on a Shimadzu 2600 UV spectrophotometer by using BaSO<sub>4</sub> as a reference.

### 2.3. Photoelectrochemical measurement of established PEC systems

We have constructed different photoelectrodes configuration-based PEC systems such as the TiO<sub>2</sub> NNs/Ti mesh photoanode coupling with Pt cathode (TiO<sub>2</sub> NNs-Pt), the Pt anode coupling with NCDs/Co<sub>3</sub>O<sub>4</sub>/Ti mesh photocathode (Pt-NCDs/Co<sub>3</sub>O<sub>4</sub>), and the TiO<sub>2</sub> NNs/Ti mesh photoanode coupling with NCDs/Co<sub>3</sub>O<sub>4</sub>/Ti mesh photocathode (TiO<sub>2</sub> NNs-NCDs/Co<sub>3</sub>O<sub>4</sub>). Two 30 W LED lamps were used as the light source. The photoelectrochemical performance of the established PEC systems was analyzed using the three-electrode system with CHI760D (Shanghai China) electrochemical station. All tests were carried out in 0.05 M Na<sub>2</sub>SO<sub>4</sub> electrolyte using Ag/AgCl as the reference electrode, Pt foil and as-prepared photoelectrode as counter electrode and working electrode, respectively. However, in the case of the TiO<sub>2</sub> NNs-NCDs/Co<sub>3</sub>O<sub>4</sub> PEC system, the TiO<sub>2</sub> NNs/Ti mesh used as the working electrode and NCDs/Co<sub>3</sub>O<sub>4</sub>/Ti mesh were considered as a counter electrode and Ag/AgCl as a reference electrode. Electrochemical impedance spectroscopy (EIS) was measured at an open-circuit voltage of 100 kHz to 0.01 Hz with or without LED lamp illumination. Mott-Schottky (MS) analysis was investigated at 1 kHz in the dark to determine the flat-band potential. The  $J-t$  curve in the process of SDZ removal was recorded in a three-electrode cell under the irradiation of LED lamp. The incident photo-to-current conversion efficiency (IPCE) (as shown in [Eq. 1](#)) was measured at a potential of 0.4 V vs. Ag/AgCl and within a wavelength of 380–840 nm [30].

$$IPCE = \frac{1240 \times J_{ph}}{\lambda \times P_{mono}} \times 100\% \quad (1)$$

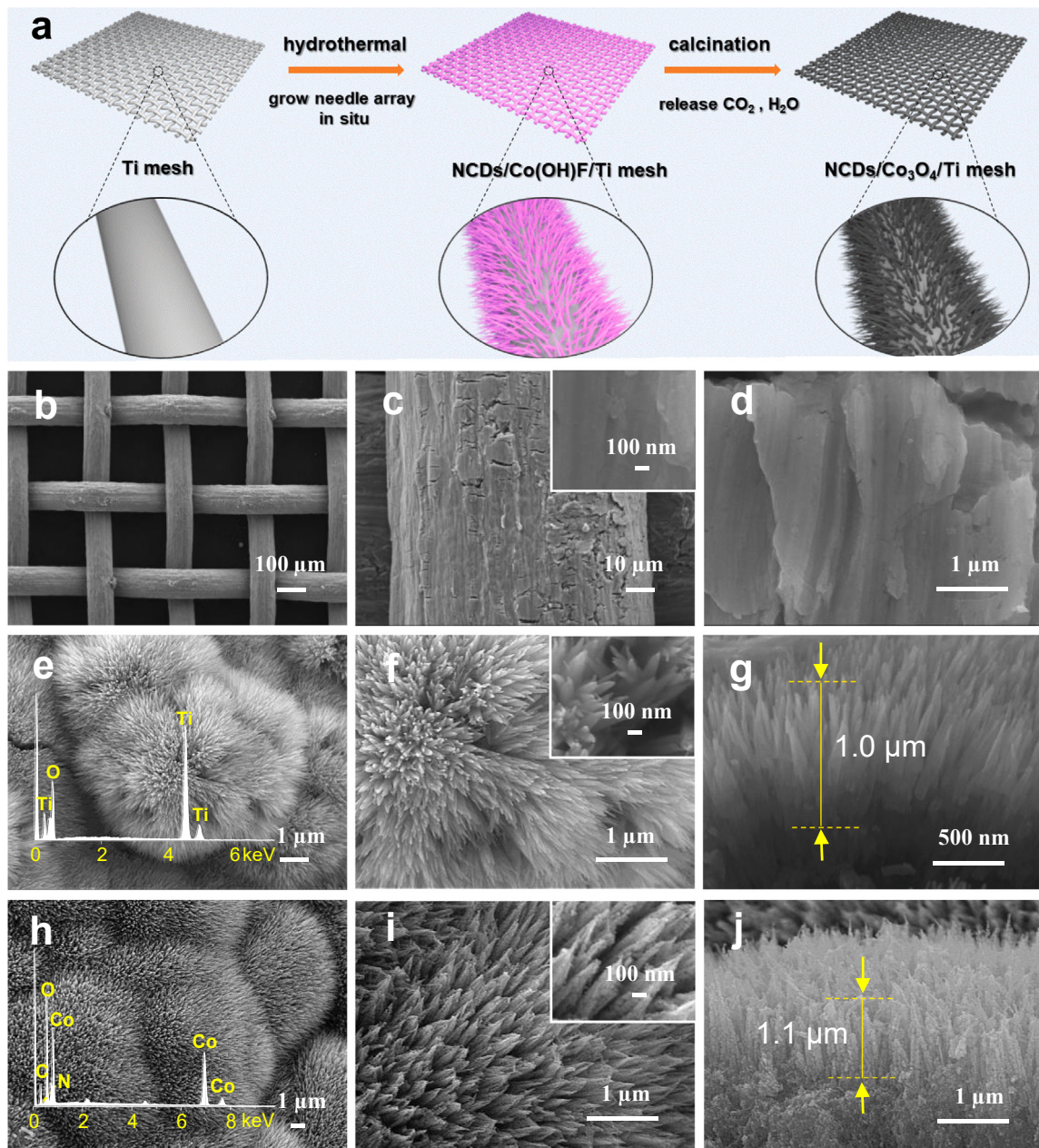


**Fig. 1.** (a) Detailed prepared diagram for NCDs/Co<sub>3</sub>O<sub>4</sub>/Ti mesh photocathode. (b-d) FESEM images of Ti mesh. (e, f) FESEM images of TiO<sub>2</sub> NPs/Ti mesh. Inset: EDS spectrum or the magnified image of TiO<sub>2</sub> NPs/Ti mesh. (g) The cross sectional FESEM image of TiO<sub>2</sub> NPs/Ti mesh. (h, i) FESEM images of NCDs/Co<sub>3</sub>O<sub>4</sub>/Ti mesh. Inset: EDS spectrum or the magnified image of NCDs/Co<sub>3</sub>O<sub>4</sub>/Ti mesh. (j) The cross sectional FESEM image of NCDs/Co<sub>3</sub>O<sub>4</sub>/Ti mesh.

where  $J_{ph}$ ,  $\lambda$ ,  $P_{mono}$  are the photocurrent density ( $\text{mA cm}^{-2}$ ), the wavelength (nm) and intensity ( $\text{mW cm}^{-2}$ ) of monochromatic light, respectively.

#### 2.4. Photoelectrocatalytic activity test

Taking SDZ ( $10 \text{ mg L}^{-1}$ ) as a model pollutant, the degradation experiments were carried out in a single-chamber electrolysis cell with two-electrode system, as shown in Fig. S1. Typically, the TiO<sub>2</sub> NPs/Ti mesh ( $2.5 \times 2.8 \text{ cm}^2$ ) and NCDs/Co<sub>3</sub>O<sub>4</sub>/Ti mesh ( $2.5 \times 2.8 \text{ cm}^2$ ) were used as the photoanode and photocathode, respectively. Before irradiation, the as-synthesized electrodes were immersed in the SDZ solution for 30 min to achieve adsorption/desorption equilibrium. Afterward, the established PEC system was irradiated with LED light along with an external voltage to start the photo-electrocatalytic reaction. Each

experiment was performed in triplicates or more.

#### 2.5. Analytical methods

The concentration of SDZ was determined by high-performance liquid chromatography (HPLC, Ultimate 3000 ThermoFisher, Acclaim<sup>TM</sup> 120 C18 column at  $30^\circ\text{C}$ , a 35:65 v/v acetonitrile/water solution as mobile phase, flow rate of  $0.5 \text{ mL min}^{-1}$ , and detection wavelength of 262 nm). The Co leaching concentration was quantified by ICP-MS (PerkinElmer ELAN DRC-e, USA). The ROS were detected by electron paramagnetic resonance (EPR, Bruker EMX Nano, Germany) by employing 5,5-dimethyl-1-pyrroline N-oxide (DMPO) as spin-trapping agent. Precisely, the hydroxyl radical ( $\cdot\text{OH}$ ) was quantified using dimethyl sulfoxide (DMSO) and 2, 4-dinitrophenylhydrazine, which would react with  $\cdot\text{OH}$  in phosphate buffer solution to produce

hydrazone [31]. The concentrations of the generated hydrazone could be quantitatively analyzed by HPLC. The super oxide radical ( $\bullet\text{O}_2^-$ ) was detected by using nitro-blue tetrazolium (NBT) molecular probe [7]. Specifically,  $\bullet\text{O}_2^-$  can react with NBT to form the insoluble formazan, and decrease the intensity of absorption peak at 259 nm.

### 2.6. DFT calculations

The calculation of the density functional theory (DFT) was performed using “Vienna Ab initio Simulation Package (VASP 5.4.1)”, which are based on the generalized gradient approximation with the Perdew-Burke-Ernzerhof (PBE) exchange and correlation functional [32–34]. A plane wave base with a cutoff energy of 400 eV and the

projection augmented wave method frame were employed. Additionally, the Gaussian smearing width was set to 0.2 eV and the Brillouin zone was set to  $3 \times 3 \times 1$  K points. All atoms were converged to 0.01 eV/Å.

## 3. Results and Discussion

### 3.1. Characterizations of photoelectrodes

The FESEM images in Fig. 1b-d confirmed that the interconnected 3D network structure of the Ti mesh substrate with numerous fine grids on its surface. As indicated in previous researches, these characteristics make Ti mesh an excellent substrate for in situ growth of catalyst with

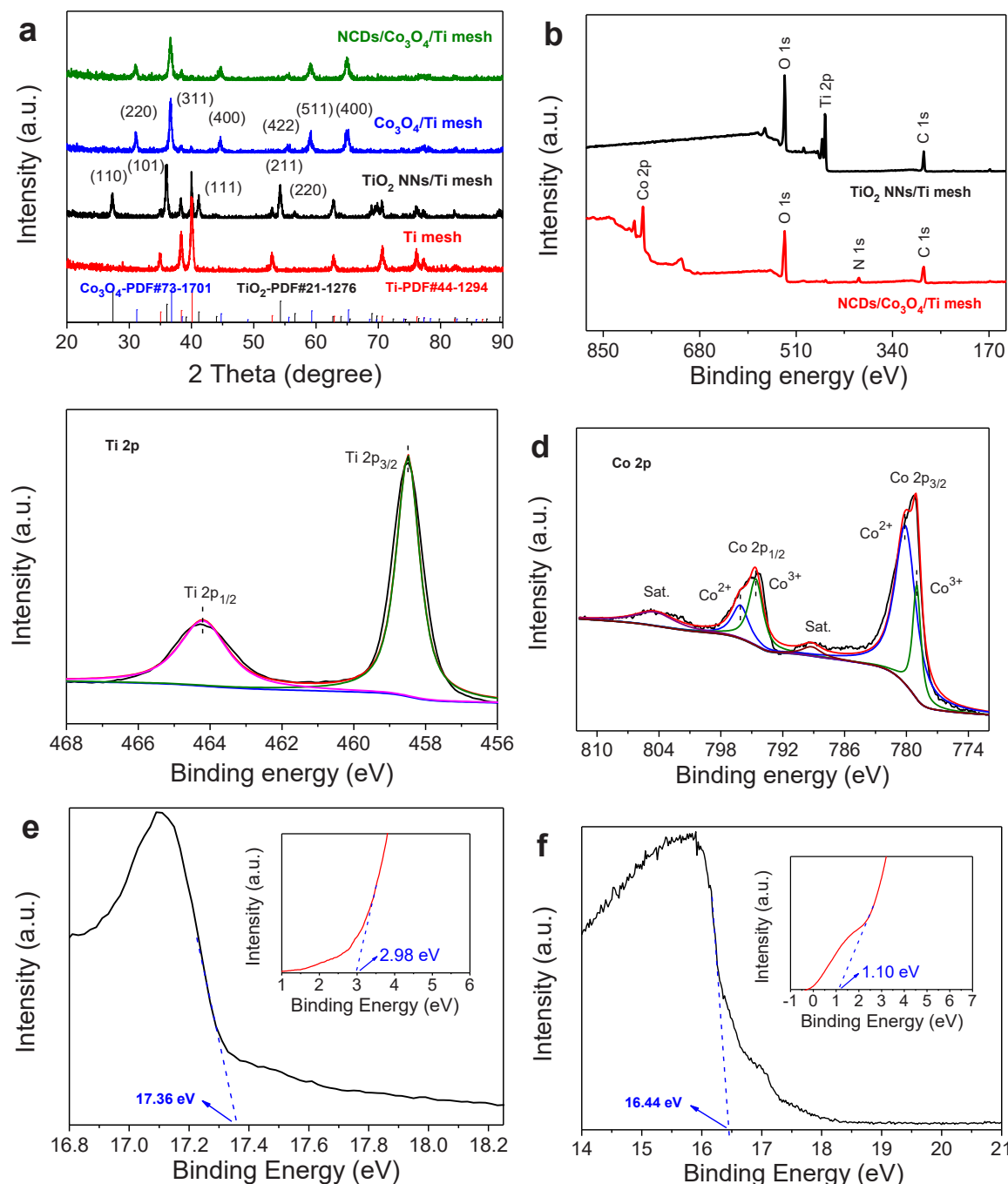


**Fig. 2.** (a) XRD patterns of TiO<sub>2</sub> NNS/Ti mesh, Co<sub>3</sub>O<sub>4</sub>/Ti mesh, NCDs/Co<sub>3</sub>O<sub>4</sub>/Ti mesh. (b) Full XPS spectra record from the surface for TiO<sub>2</sub> NNS/Ti mesh and NCDs/Co<sub>3</sub>O<sub>4</sub>/Ti mesh. High-resolution XPS spectra of (c) Ti 2p, and (d) Co 2p. UPS spectra of (e) TiO<sub>2</sub> NNS/Ti mesh and (f) NCDs/Co<sub>3</sub>O<sub>4</sub>/Ti mesh.

3D branched array structure [11,24]. The FESEM images of the as-synthesized  $\text{TiO}_2$  NNs/Ti mesh photoanode showed that the  $\text{TiO}_2$  was densely and radially grown over Ti wires to develop 3D nanoneedle array structure (Fig. 1e and f). These well-oriented  $\text{TiO}_2$  nanoneedle arrays with a length of about  $1.0\ \mu\text{m}$  (Fig. 1g) were consistent with previous literature [35]. Similarly, EDS analysis and element mapping revealed the uniform distribution of Ti and O elements on the surface of the  $\text{TiO}_2$  NNs/Ti mesh photoanode (inset of Fig. 1e and Fig. S2). Moreover, a 3D branched array structure composed of densely packed small nanoparticles over the entire surface of the Ti mesh was observed in  $\text{Co}_3\text{O}_4$ /Ti mesh (Fig. S3) [36]. The 3D branched array structure significantly developed after the incorporation of small diameter of NCDs (2–10 nm) material with  $\text{Co}_3\text{O}_4$ /Ti mesh (NCDs/ $\text{Co}_3\text{O}_4$ /Ti mesh photocathode) (Fig. 1h, i) [37]. Comparatively, the nanoarrays thickness of NCDs/ $\text{Co}_3\text{O}_4$  composite and  $\text{Co}_3\text{O}_4$  on Ti mesh were about  $1.1\ \mu\text{m}$  and  $4.6\ \mu\text{m}$ , respectively (Fig. 1j and Fig. S3d). Such differences would possibly be ascribed to the  $\text{Co}(\text{CO}_3)_{0.5}(\text{OH})0.11\ \text{H}_2\text{O}$  precursor, which was grown from  $\text{Co}_3\text{O}_4$  in the hydrothermal process, and converted to the  $\text{Co}(\text{OH})\text{F}$  precursor after incorporation of NCDs (Fig. S4) [38,39]. Moreover, EDS analysis and element mapping revealed that the Co, O, C and N were the predominant elements of the NCDs/ $\text{Co}_3\text{O}_4$ /Ti mesh photocathode, which consequently confirmed that NCDs and  $\text{Co}_3\text{O}_4$  materials had been effectively incorporated to develop novel NCDs/ $\text{Co}_3\text{O}_4$ /Ti mesh electrode (inset of Fig. 1h, Fig. S5). Interestingly, the Ti mesh was surrounded by nanoneedle-like  $\text{TiO}_2$  semiconductor or NCDs/ $\text{Co}_3\text{O}_4$  composite to constitute 3D branched structure. It has been reported that 3D interconnected network architecture possessed larger surface area, higher charge separation and transfer efficiency, and swift diffusion than planar 1D films [24,40].

The crystalline phases of the photoelectrodes were further analyzed via XRD. In Fig. 2a, the dominant diffraction the peaks of  $\text{TiO}_2$  NNs/Ti mesh at  $27.45^\circ$ ,  $36.08^\circ$ ,  $41.23^\circ$ ,  $54.32^\circ$  and  $56.64^\circ$  can be assigned to the (110), (101), (111), (211) and (220) planes of the tetragonal rutile  $\text{TiO}_2$  (JCPDS No. 21–1276) [35]. Similarly, based on the diffraction peaks of the  $\text{Co}_3\text{O}_4$ /Ti mesh, it is assumed that XRD pattern of pristine  $\text{Co}_3\text{O}_4$  was associated with a cubic structure (JCPDS No. 73–1701). Compared with the  $\text{Co}_3\text{O}_4$ /Ti mesh, there was no obvious change in peak position and intensity of NCDs/ $\text{Co}_3\text{O}_4$ /Ti mesh, which could be ascribed to the low crystallinity of NCDs [7]. In addition, the XPS was employed to investigate the composition and chemical states of the element. As exhibited in Fig. 2b, the full XPS spectrum of the  $\text{TiO}_2$  NNs/Ti mesh and the NCDs/ $\text{Co}_3\text{O}_4$ /Ti mesh agreed well with EDS and elemental mapping (Fig. S2 and Fig. S5). The high-resolution Ti 2p XPS spectrum of the  $\text{TiO}_2$  NNs/Ti mesh is displayed in Fig. 2c. The peaks centered at 458.4 eV and 464.1 eV correspond to the  $\text{Ti}^{4+}$   $2p_{3/2}$  and  $\text{Ti}^{4+}$   $2p_{1/2}$  in the  $\text{TiO}_2$  lattice, respectively [23]. For the NCDs/ $\text{Co}_3\text{O}_4$ /Ti mesh electrode, the high-resolution Co 2p, C1s, and N1s spectra are shown in Fig. 2d and Fig. S6. The prominent peaks of Co 2p spectra at binding energy of 795.5 and 780.6 eV implied the existence of Co  $2p_{1/2}$  and Co  $2p_{3/2}$  (Fig. 2d). Specifically, four Co 2p corresponding peaks at binding energy of 796.1 eV ( $\text{Co}^{2+}$ ), 794.6 eV ( $\text{Co}^{3+}$ ), 780.1 ( $\text{Co}^{2+}$ ), and 779.0 eV ( $\text{Co}^{3+}$ ) specified the existing oxidation state of Co in the NCDs/ $\text{Co}_3\text{O}_4$ /Ti mesh complex [39]. Fig. S6 shows that there are characteristic peaks of NCDs in C1s and N1s spectra, which would possibly be ascribed to the NCDs doping with  $\text{Co}_3\text{O}_4$  composite [9]. Based on above results, it could be perceived that the  $\text{TiO}_2$  NNs/Ti mesh photoanode and NCDs/ $\text{Co}_3\text{O}_4$ /Ti mesh photocathode have been successfully prepared.

The optical absorption capacity and the energy band position were also investigated according to the UV–vis DRS and UPS spectra. As demonstrated in Fig. S7a, the absorption edge and the energy band ( $E_g$ ) of  $\text{TiO}_2$  NNs/Ti mesh were located around  $412\ \text{nm}$  and  $3.01\ \text{eV}$ , respectively [23]. Furthermore, the valence band ( $E_{\text{VB}}$ ) and conduction band ( $E_{\text{CB}}$ ) were calculated using the following Eqs. 2–4 [41,42].

$$E_{\text{VB}} \text{ vs. vacuum} = - (21.22 - E_{\text{cutoff}} + E_{\text{edge}}) \quad (2)$$

$$E_{\text{VB}} \text{ vs. NHE} = - E_{\text{VB}} \text{ vs. vacuum} - 4.44\ \text{eV} \quad (3)$$

$$E_{\text{CB}} \text{ vs. NHE} = E_{\text{VB}} \text{ vs. vacuum} - E_g \quad (4)$$

where  $E_{\text{VB}}$  vs. vacuum and  $E_{\text{VB}}$  vs. NHE are the vacuum energy level and the normal hydrogen electrode potential, respectively;  $E_{\text{cutoff}}$  is the cutoff edge of secondary electron emission (eV);  $E_{\text{edge}}$  is the low-binding-energy cutoff edge (eV). According to the UPS spectra of the  $\text{TiO}_2$  NNs/Ti mesh (Fig. 2e), the  $E_{\text{cutoff}}$  of  $17.36\ \text{eV}$  and  $E_{\text{edge}}$  of  $2.98\ \text{eV}$  were used to calculate  $E_{\text{VB}}$  vs. vacuum value of  $-6.80\ \text{eV}$ . Thus, the calculated  $E_{\text{VB}}$  vs. NHE and  $E_{\text{CB}}$  vs. NHE for the  $\text{TiO}_2$  NNs/Ti mesh photoanode were around  $2.40\ \text{eV}$  and  $-0.61\ \text{eV}$ , respectively. A similar analysis was also carried out for  $\text{Co}_3\text{O}_4$ /Ti mesh, and NCDs/ $\text{Co}_3\text{O}_4$ /Ti mesh, as shown in Fig. S7b, their corresponding  $E_g$  values were estimated as  $2.33\ \text{eV}$  and  $2.39\ \text{eV}$ , respectively based on the Tauc plot equation:  $[(\alpha h\nu)^2 = A(h\nu - E_g)]$  [25]. Notably, NCDs/ $\text{Co}_3\text{O}_4$ /Ti mesh photoanode exhibits increased light absorption in both the UV–vis region compared to the  $\text{Co}_3\text{O}_4$ /Ti mesh electrode, which could be due to the light absorption effect of NCDs [23]. The UPS spectra of the NCDs/ $\text{Co}_3\text{O}_4$ /Ti mesh photoanode were plotted in Fig. 2f. Similarly, the  $E_{\text{VB}}$  and  $E_{\text{CB}}$  energy positions of the NCDs/ $\text{Co}_3\text{O}_4$ /Ti mesh photocathode were determined to be  $1.44\ \text{eV}$  and  $-0.89\ \text{eV}$  vs. NHE based on above equations. Meanwhile, the work functions of  $\text{TiO}_2$  NNs/Ti mesh and NCDs/ $\text{Co}_3\text{O}_4$ /Ti mesh have also been determined as  $3.86\ \text{eV}$  and  $4.78\ \text{eV}$  vs. vacuum (Fig. S7c). Hence, the Fermi levels ( $E_F$ ) of  $\text{TiO}_2$  NNs/Ti mesh and NCDs/ $\text{Co}_3\text{O}_4$ /Ti mesh were calculated to be  $-0.58\ \text{eV}$  and  $0.34\ \text{eV}$  vs. NHE, respectively, revealing their energy level matching [21]. The electron energy diagram of  $\text{TiO}_2$  NNs/Ti mesh photoanode and NCDs/ $\text{Co}_3\text{O}_4$ /Ti mesh photocathode in a tandem PEC cell is shown in Fig. S7d.

### 3.2. Photoelectrochemical properties

The PEC properties of  $\text{TiO}_2$  NNs-Pt, Pt-NCDs/ $\text{Co}_3\text{O}_4$  and  $\text{TiO}_2$  NNs-NCDs/ $\text{Co}_3\text{O}_4$  PEC systems were investigated using a three-electrode system. In order to confirm the type of semiconductor, the MS analysis was conducted as shown in Fig. 3a, b. It was obviously found that  $\text{TiO}_2$  NNs/Ti mesh and NCDs/ $\text{Co}_3\text{O}_4$ /Ti mesh have exhibited positive and negative slopes, respectively. Consequently, such observations highlight that the  $\text{TiO}_2$  NNs/Ti mesh is an n-type semiconductor, whereas the NCDs/ $\text{Co}_3\text{O}_4$ /Ti mesh is a p-type photocatalyst. The flat band potentials ( $E_{\text{fb}}$ ) of the  $\text{TiO}_2$  NNs/Ti mesh and the NCDs/ $\text{Co}_3\text{O}_4$ /Ti mesh were estimated to be  $-0.58\ \text{V}$  vs.  $\text{Ag}/\text{AgCl}$  and  $1.15\ \text{V}$  vs.  $\text{Ag}/\text{AgCl}$ , respectively (Eq. 5) [23].

$$\frac{1}{C^2} = \frac{2}{\epsilon \epsilon_0 e N_D} \left( E - E_{\text{fb}} - \frac{k_B T}{e} \right) \quad (5)$$

where  $C$ ,  $N_D$  are the space charge capacitance and charge carrier density,  $\epsilon_0$  and  $\epsilon$  are the permittivity of the vacuum ( $8.854 \times 10^{-12}\ \text{F m}^{-1}$ ) and the relative permittivity of the semiconductor, respectively;  $E$  (vs.  $\text{Ag}/\text{AgCl}$ ) and  $E_{\text{fb}}$  (vs.  $\text{Ag}/\text{AgCl}$ ) are the applied potential and the flat band potential, respectively,  $k_B$  is Boltzmann constant ( $1.381 \times 10^{-23}\ \text{J K}^{-1}$ );  $T$  is the absolute temperature ( $273.15\ \text{K}$ ), and  $e$  is the electron charge ( $1.602 \times 10^{-19}\ \text{C}$ ).

It is reasonable to establish dual-photoelectrode PEC system using  $\text{TiO}_2$  NNs/Ti mesh photoanode and NCDs/ $\text{Co}_3\text{O}_4$ /Ti mesh photocathode. To optimize the catalytic activity, the photocurrents of the dual-photoelectrode PEC system composed of NCDs/ $\text{Co}_3\text{O}_4$ /Ti mesh with different content of NCDs and  $\text{TiO}_2$  NNs/Ti mesh were further studied at room temperature, and the results are shown in Fig. S8. Notably, the photocurrent density of the  $\text{TiO}_2$  NNs-(0.50-)NCDs/ $\text{Co}_3\text{O}_4$  system was  $\sim 0.121\ \text{mA cm}^{-2}$ , which exhibited higher photocurrent than that of  $\text{TiO}_2$  NNs-/ $\text{Co}_3\text{O}_4$  ( $\sim 0.066\ \text{mA cm}^{-2}$ ),  $\text{TiO}_2$  NNs-(0.25-)NCDs/ $\text{Co}_3\text{O}_4$  ( $\sim 0.076\ \text{mA cm}^{-2}$ ), and  $\text{TiO}_2$  NNs-(1.00-)NCDs/ $\text{Co}_3\text{O}_4$  ( $\sim 0.086\ \text{mA cm}^{-2}$ ) PEC system. This was mainly because NCDs co-catalyst was favorable for the separation and transfer of photogenerated carriers,

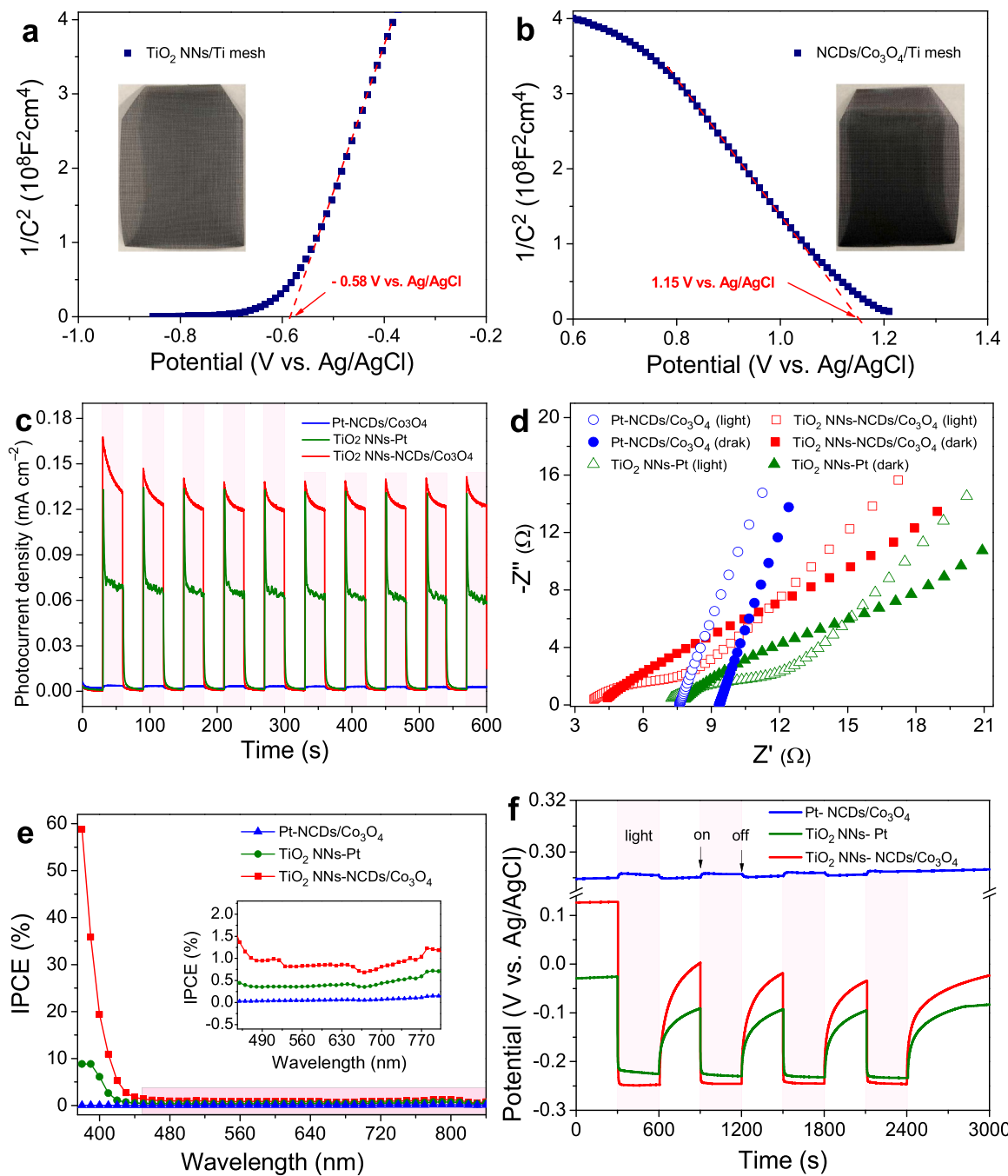


**Fig. 3.** (a) MS plots for  $\text{TiO}_2$  NNs/Ti mesh and (b) NCDs/Co<sub>3</sub>O<sub>4</sub>/Ti mesh electrodes in the dark. (c) Transient photocurrent responses. (d) EIS Nyquist plots with or without LED-light irradiation. (e) IPCE spectra and (f) Open-circuit voltage spectra of Pt-NCDs/Co<sub>3</sub>O<sub>4</sub>,  $\text{TiO}_2$  NNs-Pt and  $\text{TiO}_2$  NNs-NCDs/Co<sub>3</sub>O<sub>4</sub> PEC system.

while excessive NCDs will be the recombination center of photo-generated electrons and holes [7,29]. The result indicated that 0.50-NCDs/Co<sub>3</sub>O<sub>4</sub> was an optimal ratio of NCDs in this composite, which was most suitable for coupling with  $\text{TiO}_2$  NNs/Ti mesh photoanode. Meanwhile, Fig. 3c demonstrates that the photocurrent density of  $\text{TiO}_2$  NNs-(0.50)-NCDs/Co<sub>3</sub>O<sub>4</sub> (i.e.  $\text{TiO}_2$  NNs-NCDs/Co<sub>3</sub>O<sub>4</sub>) system is 1.90 and 40 times of that in  $\text{TiO}_2$  NNs-Pt (0.063 mA cm<sup>-2</sup>) and Pt-(0.50) NCDs/Co<sub>3</sub>O<sub>4</sub> (0.003 mA cm<sup>-2</sup>) system with single-photoelectrode, respectively. Moreover, the high-frequency arc radius on Nyquist plot with or without LED-light irradiation has been displayed in Fig. 3d. The  $\text{TiO}_2$  NNs-NCDs/Co<sub>3</sub>O<sub>4</sub> system (5.07 Ω) exhibited significantly lower charge transfer resistance as compare to the  $\text{TiO}_2$  NNs-Pt (7.29 Ω) and Pt-NCDs/Co<sub>3</sub>O<sub>4</sub> (813.80 Ω) in the light (Table S1). Consequently, the

$\text{TiO}_2$  NNs-NCDs/Co<sub>3</sub>O<sub>4</sub> PEC system had superior spatial charge transfer capacity, which would be beneficial for higher rate of ROS generation and subsequently improve the targeted pollutant degradation performance [16].

Moreover, the advanced dual-photoelectrode PEC system ( $\text{TiO}_2$  NNs-NCDs/Co<sub>3</sub>O<sub>4</sub>) also displayed superior IPCE at wavelengths of 380–840 nm (Fig. 3e). More specifically, the maximum IPCE at 380 nm of 58.8%, 8.8%, and 0.01% was observed with an application of  $\text{TiO}_2$  NNs-NCDs/Co<sub>3</sub>O<sub>4</sub>,  $\text{TiO}_2$  NNs-Pt, and Pt-NCDs/Co<sub>3</sub>O<sub>4</sub>, respectively (Fig. 3e). The reason is that the application of NCDs/Co<sub>3</sub>O<sub>4</sub>/Ti mesh as photocathode would be effective in photogenerated separation and transportation at the electrode/electrolyte interface [16,43]. Based on the above results with respect to different PEC system configurations, it

can be anticipated that the dual-photoelectrode PEC system with an NCDs/Co<sub>3</sub>O<sub>4</sub>/Ti mesh photocathode and TiO<sub>2</sub> NPs/Ti mesh photoanode would be an efficacious option to reduce the recombination of photo-generated electrons and holes. To further clarify the peculiarity of the novel TiO<sub>2</sub> NPs-NCDs/Co<sub>3</sub>O<sub>4</sub> system, the open-circuit voltage (V<sub>OC</sub>) was measured in the dark and under LED lamp irradiation. The V<sub>OC</sub> during light irradiation (V<sub>OC-light</sub>) of the TiO<sub>2</sub> NPs-Pt and Pt-NCDs/Co<sub>3</sub>O<sub>4</sub> PEC system was  $-0.221$  V vs. Ag/AgCl and  $0.292$  V vs. Ag/AgCl, whose V<sub>OC</sub> in the dark (V<sub>OC-dark</sub>) was  $-0.029$  V vs. Ag/AgCl and  $0.290$  V vs. Ag/AgCl (Fig. 3f). The V<sub>OC-light</sub> and V<sub>OC-dark</sub> were  $-0.250$  V and  $0.139$  V vs. Ag/AgCl when combined the TiO<sub>2</sub> NPs/Ti mesh photoanode with the NCDs/Co<sub>3</sub>O<sub>4</sub>/Ti mesh photocathode (Fig. 3f). From the experiments the photovoltage (V<sub>ph</sub>) was calculated by the difference between V<sub>OC-light</sub> and V<sub>OC-dark</sub> [18]. Therefore, the V<sub>ph</sub> of TiO<sub>2</sub> NPs-Pt,

Pt-NCDs/Co<sub>3</sub>O<sub>4</sub> and TiO<sub>2</sub> NPs-NCDs/Co<sub>3</sub>O<sub>4</sub> PEC system was estimated to be  $0.192$  V,  $0.002$  V and  $0.389$  V, respectively. The elevated V<sub>ph</sub> was beneficial to reduce the external voltage required by this PEC system, thus reducing the energy consumption [16,21].

### 3.3. Photoelectrochemical degradation of SDZ

To better understand the catalytic performance of different configurations of PEC system, the TiO<sub>2</sub> NPs-Pt, Pt-NCDs/Co<sub>3</sub>O<sub>4</sub>, and TiO<sub>2</sub> NPs-NCDs/Co<sub>3</sub>O<sub>4</sub> PEC systems were applied for photoelectrocatalytic removal of  $10 \text{ mg L}^{-1}$  SDZ with  $0.05 \text{ M Na}_2\text{SO}_4$ , an external voltage of  $0.4$  V, and LED light illumination. SDZ degradation kinetics were fitted with the pseudo-first-order equation, where  $k_{\text{obs}}$  is the apparent reaction rate constant. The TiO<sub>2</sub> NPs/Ti mesh photoanode and NCDs/Co<sub>3</sub>O<sub>4</sub>/Ti

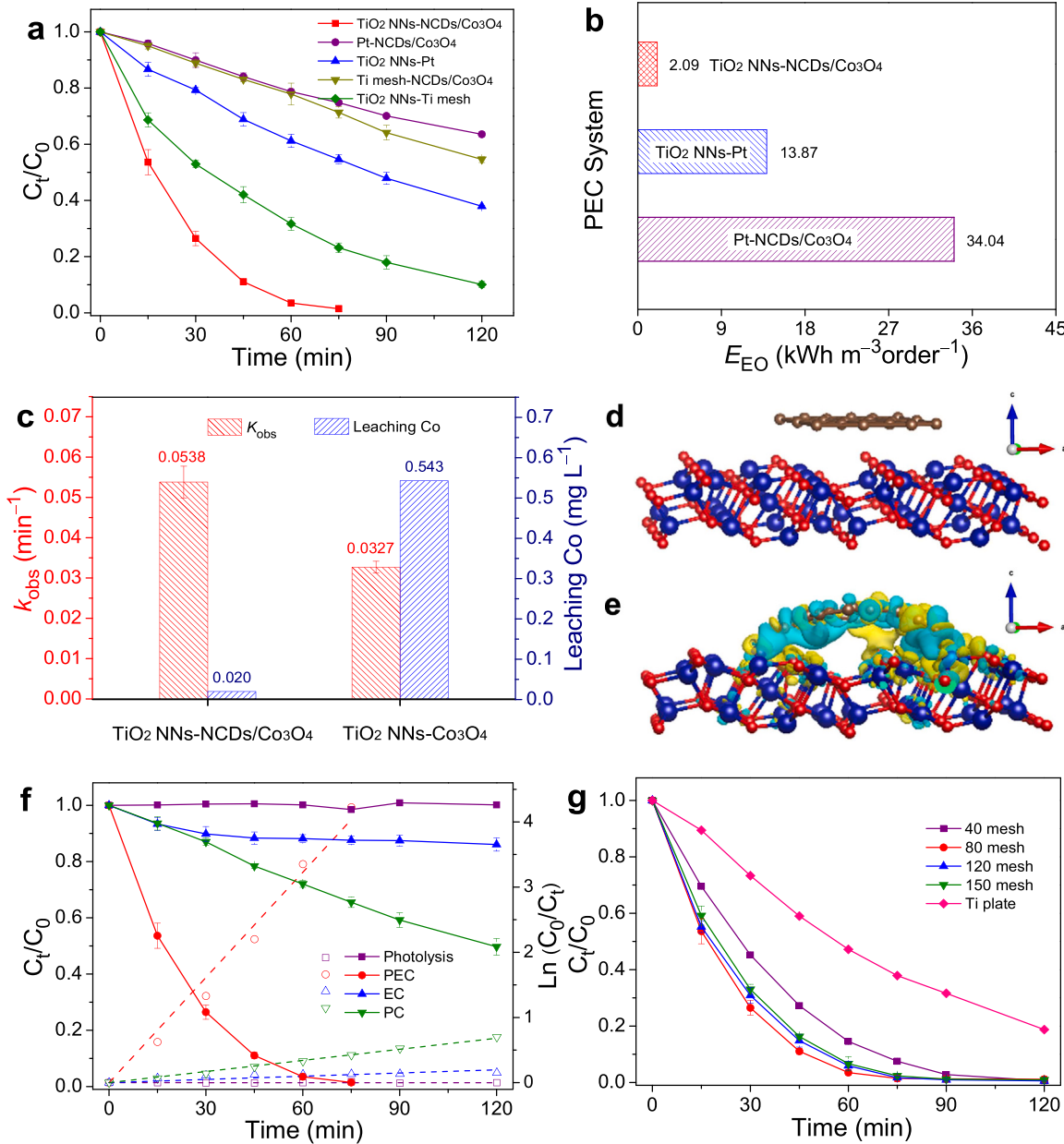


**Fig. 4.** (a) Degradation of SDZ in TiO<sub>2</sub> NPs-NCDs/Co<sub>3</sub>O<sub>4</sub>, TiO<sub>2</sub> NPs-Pt, Pt-NCDs/Co<sub>3</sub>O<sub>4</sub>, TiO<sub>2</sub> NPs-Ti mesh, Ti mesh-NCDs/Co<sub>3</sub>O<sub>4</sub> system. (b) Energy consumption ( $E_{\text{EO}}$ ) of TiO<sub>2</sub> NPs-NCDs/Co<sub>3</sub>O<sub>4</sub> and single photoelectrode PEC system for SDZ removal. (c) The  $k_{\text{obs}}$  and Co leaching concentrations after 120 min reaction at  $0.4$  V in TiO<sub>2</sub> NPs-NCDs/Co<sub>3</sub>O<sub>4</sub> and TiO<sub>2</sub> NPs-Co<sub>3</sub>O<sub>4</sub> system. (d) The crystal model of NCDs and Co<sub>3</sub>O<sub>4</sub> before contact. (e) Charge difference distribution between NCDs and Co<sub>3</sub>O<sub>4</sub> after contact (charge accumulation depicted in blue and depletion in yellow, Co: blue, O: red, NCDs: brown). (f) SDZ degradation efficiency of Photolysis and the catalytic activity of PEC, PC, and EC of TiO<sub>2</sub> NPs-NCDs/Co<sub>3</sub>O<sub>4</sub> PEC system. (g) The performance of dual-photoelectrodes prepared by network substrate and flat substrate.

mesh photocathode based dual-photoelectrode PEC system exhibited superior SDZ removal (Fig. 4a and Fig. S9). More specifically, the removal efficiency of SDZ by the  $\text{TiO}_2$  NNS-NCDs/ $\text{Co}_3\text{O}_4$  system was 98.54% ( $0.0538 \text{ min}^{-1}$ ) after 75 min of operation, and the mineralization rate of SDZ was about 70% after 360 min of reaction. However, the SDZ removal of 45.39% ( $0.0081 \text{ min}^{-1}$ ) and 25.19% ( $0.0033 \text{ min}^{-1}$ ) were observed when  $\text{TiO}_2$  NNS-Pt and Pt-NCDs/ $\text{Co}_3\text{O}_4$  were applied respectively. To investigate the influence of Ti mesh, some additional configurations of PEC systems such as  $\text{TiO}_2$  NNS/Ti mesh photoanode and Ti mesh cathode (known as  $\text{TiO}_2$  NNS-Ti mesh), Ti mesh anode and NCDs/ $\text{Co}_3\text{O}_4$ /Ti mesh photocathode (known as Ti mesh-NCDs/ $\text{Co}_3\text{O}_4$ ) were established. The results showed that the  $\text{TiO}_2$  NNS-NCDs/ $\text{Co}_3\text{O}_4$  PEC system had higher degradation efficiencies than that of  $\text{TiO}_2$  NNS-Ti mesh (76.82%,  $0.0196 \text{ min}^{-1}$ ) and Ti mesh-NCDs/ $\text{Co}_3\text{O}_4$  (28.69%,  $0.0043 \text{ min}^{-1}$ ) (Fig. 4a and Fig. S9). The main reason for substantial discrepancies in SDZ degradation could be attributed to the considerable internal  $V_{ph}$  generated by the photoexcited  $\text{TiO}_2$  NNS/Ti mesh and NCDs/ $\text{Co}_3\text{O}_4$ /Ti mesh [21]. The high  $V_{ph}$  would reduce the external energy input, and thus declining the energy consumption of PEC system. In order to justify such prediction, the energy consumption of each system was evaluated from the electrical energy per order ( $E_{EO}$ ) (Supporting Information). As can be seen from Fig. 4b and Fig. S10, the  $E_{EO}$  for the SDZ removal of  $\text{TiO}_2$  NNS-Pt, Pt-NCDs/ $\text{Co}_3\text{O}_4$  and  $\text{TiO}_2$  NNS-NCDs/ $\text{Co}_3\text{O}_4$  PEC system was about 34.04, 13.87, and  $2.09 \text{ kWh m}^{-3} \text{ order}^{-1}$ , respectively. Notably, the energy consumption of the dual-photoelectrode PEC system was significantly lower than that of the single-photoelectrode system, which was also lower than the values of previous reports [44]. It could be postulated that the novel  $\text{TiO}_2$  NNS-NCDs/ $\text{Co}_3\text{O}_4$  is an energy-efficient PEC system with high-performance. Furthermore, the activity of the  $\text{TiO}_2$  NNS- $\text{Co}_3\text{O}_4$  system was also explored. As clearly depicted in Fig. 4b and Fig. S11a, the SDZ degradation performance of  $\text{TiO}_2$  NNS- $\text{Co}_3\text{O}_4$  ( $0.0327 \text{ min}^{-1}$ ) was far inferior than that of  $\text{TiO}_2$  NNS-NCDs/ $\text{Co}_3\text{O}_4$ . The Co dissolution concentration of  $\text{TiO}_2$  NNS- $\text{Co}_3\text{O}_4$  was  $0.543 \text{ mg L}^{-1}$ , which decreased sharply to  $0.020 \text{ mg L}^{-1}$  after the addition of NCDs ( $\text{TiO}_2$  NNS-NCDs/ $\text{Co}_3\text{O}_4$ ). The reason could be that the electrons on the NCDs/ $\text{Co}_3\text{O}_4$ /Ti mesh would be transferred from  $\text{Co}_3\text{O}_4$  to NCDs, which was a good electron acceptor material [29]. In this way, the separation rate of photogenerated carriers was improved and the photocorrosion of  $\text{Co}_3\text{O}_4$  could be avoided. The DFT calculation was employed to prove the hypothesis of electron transfer in NCDs/ $\text{Co}_3\text{O}_4$  heterojunctions. It was obvious that the difference in charge density mainly occurred at the interface of NCDs/ $\text{Co}_3\text{O}_4$  and the electrons could be transferred from  $\text{Co}_3\text{O}_4$  (electron depletion) to NCDs (electron accumulation) (Fig. 4d, e) [45]. Moreover, the electron accumulation phenomena around NCDs indicated that NCDs can store and transfer electrons, which is consistent with the electron sink effect of carbon dots [23,28]. As a result, NCDs could improve the activity and stability of  $\text{TiO}_2$  NNS-NCDs/ $\text{Co}_3\text{O}_4$  PEC system due to their light absorption property and electron sink effect.

Similarly, the control experiments of dark adsorption, photocatalysis (PC) and electrocatalysis (EC) were conducted to verify the operational performance of the  $\text{TiO}_2$  NNS-NCDs/ $\text{Co}_3\text{O}_4$  PEC system. It could be seen from Fig. S11b that the novel dual-photoelectrode PEC system possessed a low adsorption capacity (8.44%, 90 min) for SDZ. Fig. 4f indicated that the  $k_{obs}$  of SDZ degradation by PEC was  $0.0538 \text{ min}^{-1}$ , which was about 9.78 and 24.45 times higher than the PC ( $0.0055 \text{ min}^{-1}$ ) and EC ( $0.0022 \text{ min}^{-1}$ ), respectively. The synergistic effects of PC and EC was perceived in the application of the dual-photoelectrode PEC system ( $\text{TiO}_2$  NNS-NCDs/ $\text{Co}_3\text{O}_4$ ), resulting in an increase in SDZ removal. The LED light was efficiently absorbed and utilized by the photoelectrode to generate the carriers (PC), which were instantly separation and directional migration via external voltage (EC). Besides, it has been reported that the 3D branched array structure of catalyst is be beneficial for ample mass transport of the contaminant [11,40]. The commonly used interconnected 3D network substrates were carbon cloth and Ti mesh [24,46]. Compared with carbon cloth, Ti mesh is a promising substrate

because of its mechanical properties, which could directly load catalyst. In this work, different types of Ti substrates (e.g., Ti 40 mesh, Ti 80 mesh, Ti 120 mesh, Ti 150 mesh, and Ti plate) were used for photoelectrode synthesis. The SDZ removal performance of dual-photoelectrodes based PEC system prepared by different Ti substrates was also investigated. Fig. 4g shows that the SDZ degradation efficiency were 92.50%, 98.54%, 98.29%, 97.66% and 62.10% for Ti 40 mesh, Ti 80 mesh, Ti 120 mesh, Ti 150 mesh, and Ti plate based  $\text{TiO}_2$  NNS-NCDs/ $\text{Co}_3\text{O}_4$ , respectively. Compared to traditional Ti planar substrate ( $0.0123 \text{ min}^{-1}$ ), 3D interconnected Ti mesh-based photoelectrodes exhibited higher SDZ degradation kinetics (Fig. S12). This primary reason for such generous inequalities might be ascribed to the efficient interfacial mass transfer of pollutant via microfluidic channels of the 3D network structure [40]. To the best of our knowledge, the  $k_{obs}$  of  $\text{TiO}_2$  NNS-NCDs/ $\text{Co}_3\text{O}_4$  PEC system with interconnected 3D network structure for SDZ removal was  $0.0538 \text{ min}^{-1}$ , which was dramatically better than ever reported (Table S2).

### 3.4. Effect of parameters in the PEC process

#### 3.4.1. Applied voltage

Generally, the applied voltage has been shown one of the most persuading operative factors of the PEC system for targeted contaminants abatement [12]. More precisely, higher voltage would significantly improve the pollutant degradation potential of PEC however it will consequently increase the  $E_{EO}$  of the PEC system [11,47]. The bare PC, the self-driven  $\text{TiO}_2$  NNS-NCDs/ $\text{Co}_3\text{O}_4$  PEC, and  $\text{TiO}_2$  NNS-NCDs/ $\text{Co}_3\text{O}_4$  PEC diverse voltage (e.g., 0.2, 0.4, 0.6, 0.8, and 1.0 V) were investigated to better understand the excellent performance of the novel PEC system (Fig. 5a). The  $\text{TiO}_2$  NNS/Ti mesh photoanode and the NCDs/ $\text{Co}_3\text{O}_4$ /Ti mesh photocathode that were connected via Cu wire without applied voltage were defined as self-driven PEC system. Interestingly, the  $k_{obs}$  ( $0.0221 \text{ min}^{-1}$ ) of the self-driven system was significantly better than the bare PC. This is because the dual-photoelectrode PEC system could generate stable internal  $V_{ph}$  ( $0.389 \text{ V}$ ), which was used as a driving force to separate photogenerated carries. Thus, the novel  $\text{TiO}_2$  NNS-NCDs/ $\text{Co}_3\text{O}_4$  PEC system could be conceivably operated spontaneously without external voltage. With an application of external voltage, the  $k_{obs}$  value improved drastically to  $0.0343 \text{ min}^{-1}$  (0.2 V) and  $0.0538 \text{ min}^{-1}$  (0.4 V), which can be due to the synergistic effect of PC and EC. Nevertheless, with increasing the voltage from 0.4 V to 1.0 V, the photocurrent increased accordingly but the SDZ degradation efficiencies remained almost unchanged (Fig. S13). Such disparity can be ascribed to the consequences of the oxygen evolution reaction [11]. In order to study the variation of the operating potential of the  $\text{TiO}_2$  NNS/Ti mesh photoanode and NCDs/ $\text{Co}_3\text{O}_4$ /Ti mesh photocathode, the anodic potential (three-electrode system) and the cathodic potential (three-electrode system) under different bias potential (two-electrode system) were further monitored by a multimeter (Fig. 5b and Table S3). Notably, at the voltage of 0.4 V, the anodic potential was only 0.10 V vs. Ag/AgCl, which to the best of our knowledge was the lowest anodic potential among reported  $\text{TiO}_2$ -based PEC system (Table S4). Therefore, the application of the NCDs/ $\text{Co}_3\text{O}_4$ /Ti mesh photocathode significantly reduced the anodic potential required by  $\text{TiO}_2$ -based photoanode in water purification, which was beneficial to reduce the electric energy consumption.

To illustrate the affection paths of the applied voltage, the detailed schemes are shown in Fig. 5c and d. The  $E_{F,hole}$  and  $E_{F,electron}$  refer to the quasi-Fermi level of non-equilibrium hole and electron under illumination, which are split by the  $E_F$  of semiconductor [9]. The photovoltage ( $V_{ph}$ ) refers to the gradient of  $E_{F,hole}$  and  $E_{F,electron}$  [18]. As shown in Fig. 5c, after immersing the  $\text{TiO}_2$  NNS/Ti mesh photoanode and the NCDs/ $\text{Co}_3\text{O}_4$ /Ti mesh photocathode in the electrolyte contained PEC reactor, an rapid electron conveyance occurred (to reach equilibrium) between the photoelectrodes and the electrolyte due to the significant disparity of their  $E_F$  and  $E_{redox}$  level [9]. This phenomenon would rise to

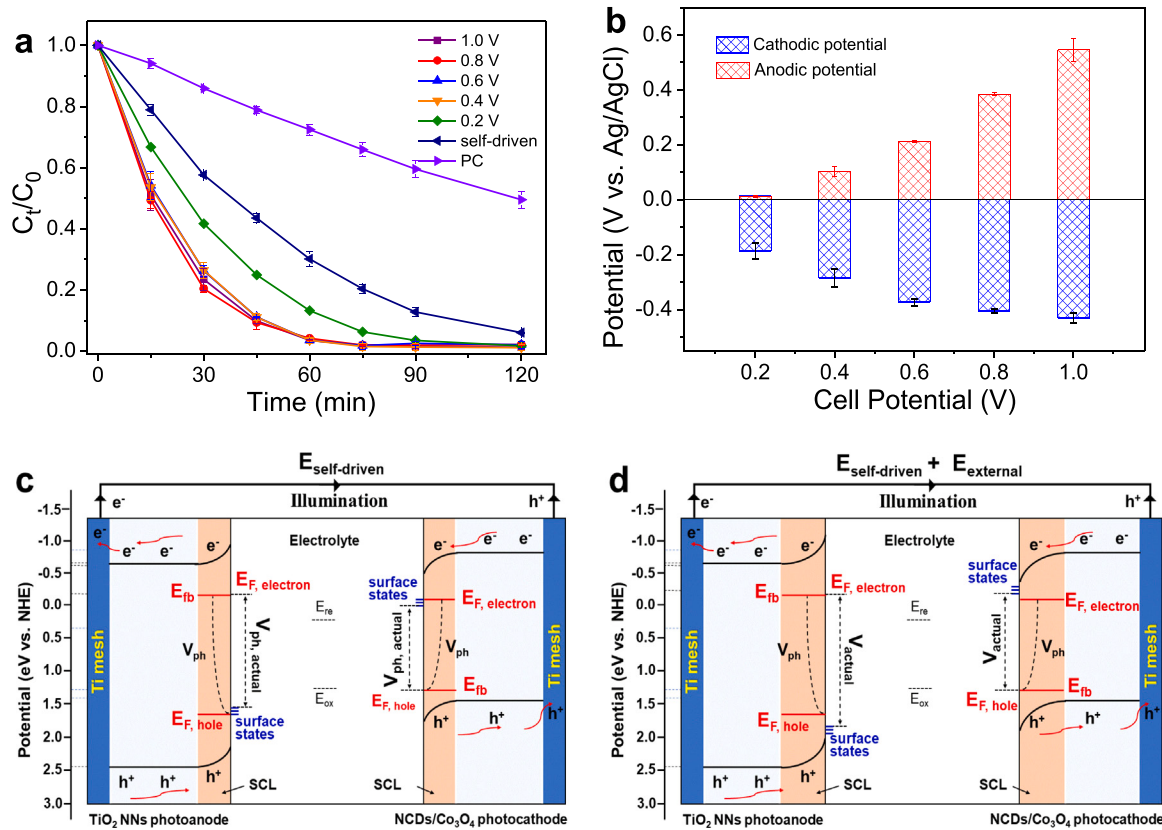


**Fig. 5.** (a) The effect of different voltage on SDZ removal in  $\text{TiO}_2$  NNS-NCDs/Co<sub>3</sub>O<sub>4</sub> system. (b) The variation of anodic potential and the cathodic potential as a function of cell voltage. Schematic diagram of semiconductor/electrolyte in a dual-photoelectrode system (c) without applied voltage and (d) with external voltage.

upward band bending of the  $\text{TiO}_2$  NNS/Ti mesh photoanode or downward band bending of the NCDs/Co<sub>3</sub>O<sub>4</sub>/Ti mesh photocathode, respectively [9]. Under the LED lamp irradiation, the produced  $E_{\text{F},\text{electron}}$  of the  $\text{TiO}_2$  NNS/Ti mesh photoanode formed and was near to  $E_{\text{fb}}$ , which was considered as the same energy potential for simplicity of this work. The  $E_{\text{F},\text{hole}}$  of the  $\text{TiO}_2$  NNS/Ti mesh photoanode was shifted downward, contributing to the generation of anodic  $V_{\text{ph}}$  [9,48]. In contrast, the  $E_{\text{F},\text{hole}}$  of the NCDs/Co<sub>3</sub>O<sub>4</sub>/Ti mesh photocathode was close to  $E_{\text{fb}}$  and the  $E_{\text{F},\text{electron}}$  was shifted upward, which would lead to produce cathodic  $V_{\text{ph}}$ . Nevertheless, the actual photovoltage ( $V_{\text{ph},\text{actual}}$ ) of photoanode or photocathode was generally lower than the ideal  $V_{\text{ph}}$ , which could attribute to the formation of surface states on the photoelectrode surface [22]. In this regard, the overall potential of self-driven ( $E_{\text{self-driven}}$ ) was equal to the sum of  $V_{\text{ph},\text{actual}}$  obtained from two photoelectrodes. However, Fig. 5a, b suggest that the  $\text{TiO}_2$  NNS-NCDs/Co<sub>3</sub>O<sub>4</sub> PEC system without external voltage has limited SDZ removal capacity (79.67%, 75 min), possibly because the  $E_{\text{self-driven}}$  was not enough to drive photoinduced carriers efficient separation and transfer. In PEC system, an external voltage has usually been required to increase the driving force [49]. After applying the required voltage in this novel dual-photoelectrode PEC system, the actual voltages ( $V_{\text{actual}}$ ) between the photoelectrodes and the reaction solution were reasonably higher than the  $V_{\text{ph}}$  of the system, resulting in thicker space charge layer (SCL) and larger band bending (Fig. 5d). In this case, the dual-photoelectrode PEC system exhibited sufficient force to separate the photogenerated carriers, improving the performance of SDZ removal. Overall, the  $V_{\text{ph}}$  produced by the photoexcited  $\text{TiO}_2$  NNS/Ti mesh photoanode and the NCDs/Co<sub>3</sub>O<sub>4</sub>/Ti mesh photocathode would adequately lower the external energy supply of the  $\text{TiO}_2$  NNS-NCDs/Co<sub>3</sub>O<sub>4</sub> PEC system in comparison with a conventional single-photoelectrode PEC system.

#### 3.4.2. Initial pH

Wastewater pH is known as one of the most important parameters that limits the efficiency of PEC technology [12,47]. Therefore, diverse initial pH values were used to investigate appropriate pH range for the novel  $\text{TiO}_2$  NNS-NCDs/Co<sub>3</sub>O<sub>4</sub> PEC system (Fig. 6a and Fig. S14a). At different pH values (5.00 – 10.00), the photocurrent density ( $\sim 0.11 \text{ mA cm}^{-2}$ ) slightly changed and the SDZ degradation efficiency reached more than 95% within 75 min, indicating that the  $\text{TiO}_2$  NNS-NCDs/Co<sub>3</sub>O<sub>4</sub> PEC system possess superior activity. Although the photocurrent density and degradation efficiency were similar, the  $k_{\text{obs}}$  of SDZ decomposition followed the order: pH 6.00 > pH 7. 00  $\approx$  pH 5.00 > pH 8.00 > pH 9.00 > pH 10.00, as shown in Fig. 6a. Combined with part 3.5,  $\cdot\text{OH}$  was the predominant ROS in  $\text{TiO}_2$  NNS-NCDs/Co<sub>3</sub>O<sub>4</sub> PEC cell. According to the Nernst equation, the acidic conditions has always displayed higher oxidative potentials of  $\cdot\text{OH}$  than alkaline medium [50]. Thus, the SDZ degradation efficiency is relatively lower under alkaline conditions. Moreover, the changes in the pH of solution during the degradation process were due to the production of low molecular weight acids (Fig. S14b) [16].

#### 3.4.3. Background constituents

The influences of widespread anions ( $\text{Cl}^-$ ,  $\text{NO}_3^-$ ,  $\text{CO}_3^{2-}$ ,  $\text{HCO}_3^-$ ) and dissolved organic matter (DOM, HA represents DOM) on the photoelectrocatalytic degradation of SDZ were also investigated. Based on the background composition of the actual water environment, the concentration of  $\text{Cl}^-$ ,  $\text{CO}_3^{2-}$  and  $\text{HCO}_3^-$  anions introduced into the system was 10 mM, and the concentration of  $\text{NO}_3^-$  anions and HA was 10 mg L<sup>-1</sup>. As illustrated in Fig. 6b, the  $k_{\text{obs}}$  extensively was decreased to  $0.0470 \text{ min}^{-1}$ ,  $0.0230 \text{ min}^{-1}$  and  $0.0260 \text{ min}^{-1}$  in the presence of  $\text{NO}_3^-$ ,  $\text{CO}_3^{2-}$ , and  $\text{HCO}_3^-$ , respectively. The SDZ corresponding degradation efficiencies decreased by 0.79% ( $\text{NO}_3^-$ ), 15.16% ( $\text{CO}_3^{2-}$ ), and 15.52% ( $\text{HCO}_3^-$ ), respectively, as shown in Fig. S15a. To begin with,  $\text{NO}_3^-$  had a

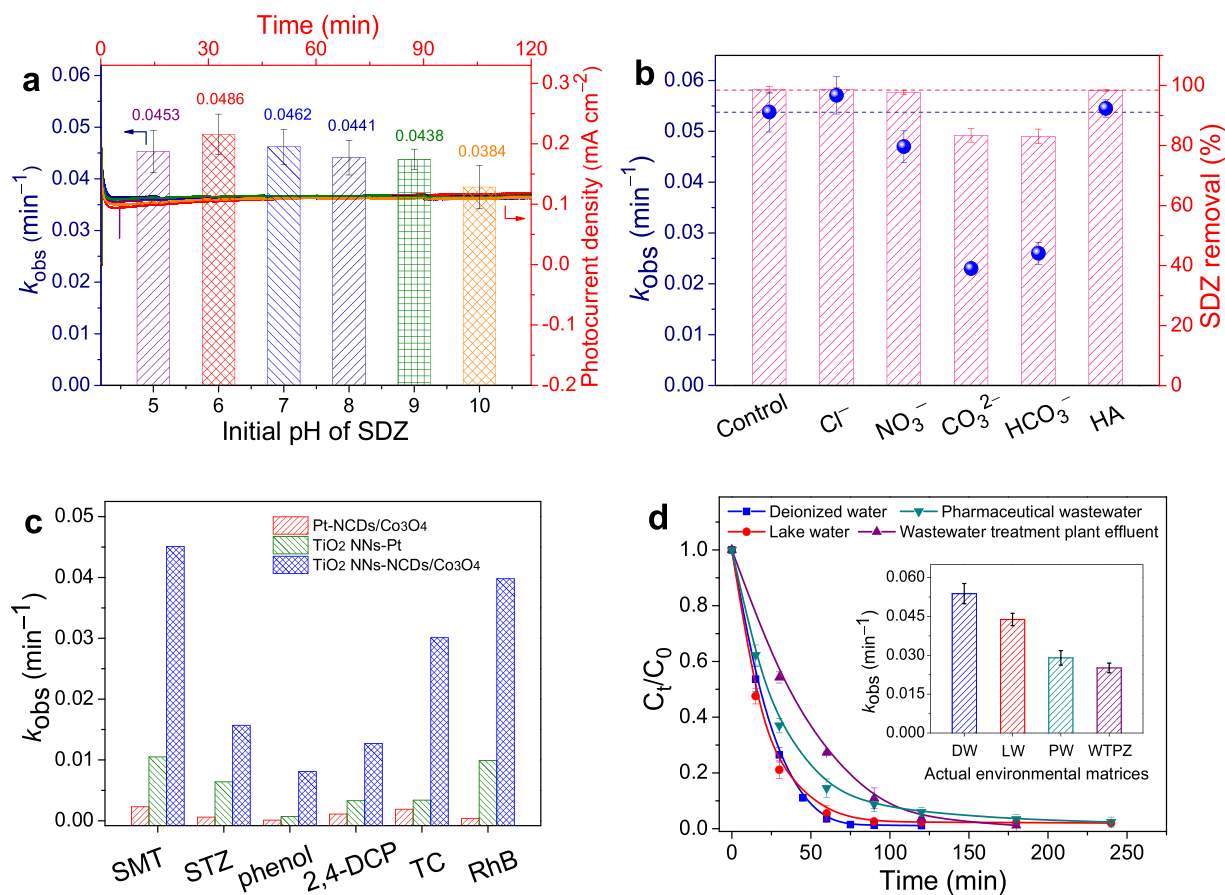
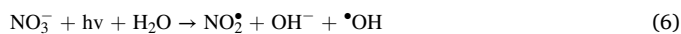


**Fig. 6.** The influences of (a) initial pH, (b) anions and HA on SDZ degradation in TiO<sub>2</sub> NNS-NCDs/Co<sub>3</sub>O<sub>4</sub> system, (c) PEC degradation of different contaminant in the Pt-NCDs/Co<sub>3</sub>O<sub>4</sub>, TiO<sub>2</sub> NNS-Pt and TiO<sub>2</sub> NNS-NCDs/Co<sub>3</sub>O<sub>4</sub> system, (d) PEC degradation of SDZ in different water matrices using TiO<sub>2</sub> NNS/Ti mesh photoanode and NCDs/Co<sub>3</sub>O<sub>4</sub>/Ti mesh photocathode.

slight detrimental effect on SDZ removal, which ascribed to the offset of dual effect. Concretely, NO<sub>3</sub><sup>-</sup> could be activated to form NO<sub>2</sub><sup>•</sup> and •OH under light illumination, which would increase the concentration of ROS in the system, resulting in increased removal of organic pollutants (Eq. 6) [51]. Meanwhile, NO<sub>3</sub><sup>-</sup> was also able to adsorb photons and be converted into NO<sub>2</sub><sup>•</sup> that could consume •OH (Eqs. 7 and 8), thus inhibiting the degradation of pollutants [52]. In TiO<sub>2</sub> NNS-NCDs/Co<sub>3</sub>O<sub>4</sub> system, the inhibitory effect of NO<sub>2</sub><sup>•</sup> was stronger than the production of NO<sub>2</sub><sup>•</sup>/•OH, so the catalytic activity of this system slightly decreased during the degradation of SDZ. Unlike NO<sub>3</sub><sup>-</sup>, SDZ degradation was markedly impeded after the addition of 10 mM of CO<sub>3</sub><sup>2-</sup> or HCO<sub>3</sub><sup>-</sup>, which was mainly due to the consumption of •OH by CO<sub>3</sub><sup>2-</sup>/HCO<sub>3</sub><sup>-</sup> [51,53]. Conversely, the Cl<sup>-</sup> ions improved the  $k_{obs}$  of SDZ degradation from 0.0538 min<sup>-1</sup> to 0.0571 min<sup>-1</sup>. This promotion phenomenon was due to the fact that Cl<sup>-</sup> ions could react with h<sup>+</sup>/•OH to produce reactive chlorine species (•Cl, •OCl and HOCl), which was about 0.564 μmol (as Cl<sub>2</sub>) after 75 min reaction (Fig. S15b) [54]. The co-existence of HA has a stimulatory effect similar to that of Cl<sup>-</sup> ions for the following reasons: i) the dissolving organic matter (HA) could react with •OH to generate DOM<sup>•</sup> ROS that could be used for targeted contaminants degradation (Eq. 9), ii) the aniline nitrogen in SDZ molecules possibly occur additional addition reactions at the electron-poor sites of DOM [55].



### 3.4.4. Different contaminants and water matrices

Despite the high activity of the dual-photoelectrode in SDZ removal, an outstanding PEC system should be versatile to remove multiple pollutants. It can be seen from Fig. S16 that TiO<sub>2</sub> NNS-NCDs/Co<sub>3</sub>O<sub>4</sub> PEC system has presented excellent performance for the degradation of sulfamethazine (SMT, 98.17%, 120 min), sulfathiazole (STZ, 99.70%, 180 min), phenol (93.96%, 240 min), 2, 4-dichlorophenol (2,4-DCP, 97.40%, 180 min), tetracycline (TC, 99.63%, 120 min) and rhodamine B (RhB, 99.03%, 120 min). Notably, the degradation ability of TiO<sub>2</sub> NNS-NCDs/Co<sub>3</sub>O<sub>4</sub> on diverse organic compounds was obviously higher than that of single-photoelectrode PEC system, which further indicated that coupling TiO<sub>2</sub> NNS photoanode and NCDs/Co<sub>3</sub>O<sub>4</sub> photocathode was a feasible way to improve the activity of PEC system. As compared to the removal efficiencies of the targeted contaminants, the apparent reaction rate constants ( $k_{obs}$ ) showed considerable variability (Fig. 6c). A possible justification for such disparity would be that the chemical structure of the pollutants could influence their intrinsic highest occupied molecular orbital ( $E_{HOMO}$ ), lowest unoccupied molecular orbital ( $E_{LUMO}$ ), and vertical ionization potential (VIP), thus affecting the decomposition pathways and degradation rates [56]. Moreover, the impacts of actual environmental matrices on the activity of the TiO<sub>2</sub> NNS-NCDs/Co<sub>3</sub>O<sub>4</sub> PEC cell were also studied, and the quality parameters of actual environmental matrices were listed in Table S5. After 120 min reaction, the TiO<sub>2</sub> NNS-NCDs/Co<sub>3</sub>O<sub>4</sub> PEC cell showcased 97.66%, 96.31%, and 94.04% removal of SDZ in lake water (LW), wastewater treatment plant effluent (WTPE) and pharmaceutical wastewater (PW), respectively (Fig. 6d). The slight inhibitory action of actual environmental matrices

might be due to the consumption of ROS by its complex components (such as  $\text{NO}_3^-$ , DOM).

### 3.5. Mechanism in the $\text{TiO}_2$ NNS-NCDs/ $\text{Co}_3\text{O}_4$ system

In PEC systems, two possible pathways (e.g., direct hole transfer and indirect  $\cdot\text{OH}$  oxidation) have been reported to degrade the targeted pollutant [10,30]. To identify the main pathway of SDZ degradation, we

have performed trapping experiments with different scavengers in the novel  $\text{TiO}_2$  NNS-NCDs/ $\text{Co}_3\text{O}_4$  PEC system. Herein, isopropanol (IPA) was served as  $\cdot\text{OH}$  scavengers due to its low light absorptivity, negligible influence on pH, and high reactivity with  $\cdot\text{OH}$  ( $k_{\cdot\text{OH}} = 2 \times 10^{9.28} \text{ M}^{-1} \text{ s}^{-1}$ ) [57]. Ethylenediaminetetraacetic acid disodium (Na<sub>2</sub>EDTA) and K<sub>2</sub>Cr<sub>2</sub>O<sub>7</sub> were used as  $\cdot\text{h}^+$  and  $\text{e}^-$  quenchers, respectively [7]. Superoxide dismutase (SOD) scavenger and the argon-purging experiment were applied to shield the effect of  $\cdot\text{O}_2^-$  [58]. As shown in Fig. 7a and

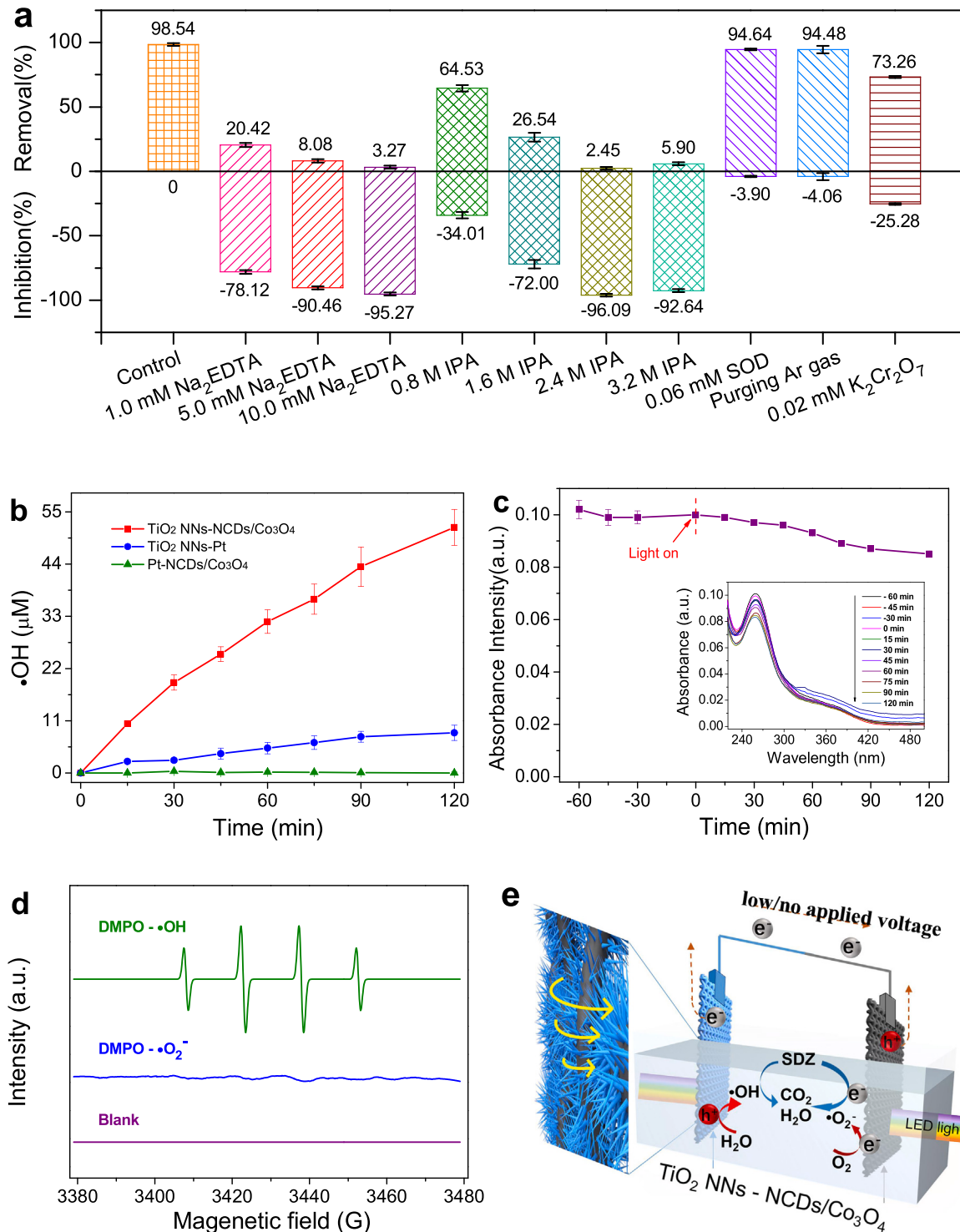


**Fig. 7.** (a) Active species trapping experiments for the SDZ degradation in  $\text{TiO}_2$  NNS-NCDs/ $\text{Co}_3\text{O}_4$  system. (b) The accumulative concentration of  $\cdot\text{OH}$  over time in different PEC systems. (c) Determination of  $\cdot\text{O}_2^-$  by NBT in  $\text{TiO}_2$  NNS-NCDs/ $\text{Co}_3\text{O}_4$  system. (d) EPR spectra of  $\text{TiO}_2$  NNS-NCDs/ $\text{Co}_3\text{O}_4$  PEC system at 30 min (e) Schematic illustration of SDZ degradation by  $\text{TiO}_2$  NNS-NCDs/ $\text{Co}_3\text{O}_4$  PEC system.

**Fig. S17**, the degradation efficiencies have abruptly been decreased with an increase of Na<sub>2</sub>EDTA and IPA concentration. However, a very slight change in SDZ degradation was observed with an excessive Na<sub>2</sub>EDTA (> 5.0 mM) and IPA (> 2.4 M). More specifically, the degradation efficiency of SDZ was 3.27% when Na<sub>2</sub>EDTA was added in TiO<sub>2</sub> NNs-NCDs/Co<sub>3</sub>O<sub>4</sub> system. This indicates that h<sup>+</sup> plays an important role in the oxidative degradation of SDZ. Meanwhile, the degradation efficiency also decreased sharply to 5.90% after adding IPA as the •OH scavenger, which was much the same as the effect of shielding h<sup>+</sup>. It was well known that •OH is formed by the reaction of the valence band h<sup>+</sup> with H<sub>2</sub>O or OH<sup>-</sup> [12]. Hence, it could be inferred that •OH was the main ROS for SDZ degradation in the TiO<sub>2</sub> NNs-NCDs/Co<sub>3</sub>O<sub>4</sub> PEC system, where h<sup>+</sup> was responsible for the oxidation of OH<sup>-</sup>/H<sub>2</sub>O to •OH. Thus, the indirect •OH oxidation was the predominant pathway to degrade SDZ in the novel dual-photoelectrode PEC system [30,59]. Additionally, 94.64% and 94.48% SDZ were decomposed after adding SOD or purging argon (Ar) gas, respectively (Fig. 7a), suggesting •O<sub>2</sub><sup>-</sup> had a very slight contribution (~ 3.9%) to the degradation of SDZ. Moreover, for K<sub>2</sub>Cr<sub>2</sub>O<sub>7</sub> with color, we chose the concentration of 0.02 mM to avoid shading effect. After the addition of K<sub>2</sub>Cr<sub>2</sub>O<sub>7</sub>, the removal efficiency was suppressed to 73.26%. Thus, the contribution of different ROS to SDZ removal in the TiO<sub>2</sub> NNs-NCDs/Co<sub>3</sub>O<sub>4</sub> PEC system was in the order: •OH > e<sup>-</sup> > •O<sub>2</sub><sup>-</sup> (Fig. S17e).

The •OH concentration produced in different PEC systems was also quantified. Reasonably, 51.76 μM of •OH was produced by TiO<sub>2</sub> NNs-NCDs/Co<sub>3</sub>O<sub>4</sub> within 120 min, which was much higher than in the TiO<sub>2</sub> NNs-Pt (8.451 μM) and Pt-NCDs/Co<sub>3</sub>O<sub>4</sub> (0.002 μM) PEC systems (Fig. 7b). The primary reason for the better •OH generation of dual-photoelectrode PEC system would be attributed to the sizable photovoltage produced between TiO<sub>2</sub> NNs/Ti mesh photoanode and NCDs/Co<sub>3</sub>O<sub>4</sub> photocathode, which could indubitably be beneficial for the separation and transportation of photocarriers, and thus produce more ROS. Besides, the absorption peak of NBT at 259 nm slightly decreased with increasing reaction time (Fig. 7c), revealing that a very small amount of •O<sub>2</sub><sup>-</sup> was also produced during SDZ removal. Persuasively, the photogenerated electrons were migrated to the NCDs/Co<sub>3</sub>O<sub>4</sub>/Ti mesh photocathode via the sum of photovoltage and external voltage, thus inhibited the formation of •O<sub>2</sub><sup>-</sup> [30,40]. The obtained results were highly consistent with the ERP analysis, indicating that •OH induces the degradation of SDZ in the TiO<sub>2</sub> NNs-NCDs/Co<sub>3</sub>O<sub>4</sub> PEC system (Fig. 7d and Fig. S18).

The mechanism of TiO<sub>2</sub> NNs-NCDs/Co<sub>3</sub>O<sub>4</sub> PEC system is shown in Fig. 7e. In short, photovoltage (V<sub>ph</sub>) was produced due to the potential difference of quasi-Femi energy between the TiO<sub>2</sub> NNs/Ti mesh photoanode and the NCDs/Co<sub>3</sub>O<sub>4</sub>/Ti mesh photocathode. Then, the photoinduced electrons of TiO<sub>2</sub> NNs/Ti mesh were swiftly transferred to NCDs/Co<sub>3</sub>O<sub>4</sub>/Ti mesh driven by V<sub>ph</sub>, and improved the separation rate of electron-hole pairs. The photoelectrons on NCDs/Co<sub>3</sub>O<sub>4</sub>/Ti mesh photocathode can be captured by the NCDs cocatalyst due to the electron sink effect of NCDs [28], which avoided the reaction of photoelectrons with the Co<sub>3</sub>O<sub>4</sub> component in the electrode. The photoelectrons accumulated on NCDs could reduce pollutant by direct electron transfer reaction or indirect generation of •O<sub>2</sub><sup>-</sup> [13,60], which was further verified by SDZ removal in the cathode chamber of two-chamber cell (Fig. S19). The corresponding holes (2.40 eV vs. NHE) of TiO<sub>2</sub> NNs/Ti mesh would remain and oxidize H<sub>2</sub>O/OH<sup>-</sup> to •OH (1.55 ≤ E ≤ 2.38 eV vs. NHE) [59], causing the efficient oxidation of contaminants. Additionally, at a low external voltage, the driving force to separate photogenerated electrons and holes became much stronger, and more photogenerated electrons and holes would be effectively involved in the decomposition of SDZ molecules.

### 3.6. Evaluation of TiO<sub>2</sub> NNs-NCDs/Co<sub>3</sub>O<sub>4</sub> in practical applications

Cycling tests were performed to evaluate the durability of the novel

TiO<sub>2</sub> NNs-NCDs/Co<sub>3</sub>O<sub>4</sub> PEC system. Based on the extensive durability evaluation, it was observed that even after 20 cycles the TiO<sub>2</sub> NNs-NCDs/Co<sub>3</sub>O<sub>4</sub> system still displayed negligible attenuation in SDZ degradation (e.g., 97.40%, 0.0527 min<sup>-1</sup>) (Fig. 8a). Consequently, it unveiled the long-term stability of novel TiO<sub>2</sub> NNs-NCDs/Co<sub>3</sub>O<sub>4</sub> PEC system. To highlight the exceptional stability of TiO<sub>2</sub> NNs-NCDs/Co<sub>3</sub>O<sub>4</sub> PEC system, the J-t curves were also monitored during recycling test. As shown in Fig. 8b, the photocurrent density (~ 0.12 mA cm<sup>-2</sup>) during SDZ removal was remained almost unchanged during twenty cycles. In addition, the FE-SEM, XRD patterns, and XPS of TiO<sub>2</sub> NNs/Ti mesh photoanode or NCDs/Co<sub>3</sub>O<sub>4</sub>/Ti mesh photocathode before and after 20 cycles were displayed significantly negligible changes with respect to their physicochemical properties (Fig. S20). The applicability of TiO<sub>2</sub> NNs-NCDs/Co<sub>3</sub>O<sub>4</sub> PEC system under real outdoor sunlight illumination was also investigated and the device diagrams are shown in Fig. S21. Under the real sunlight irradiation and no external voltage condition, this novel dual-photoelectrode PEC system demonstrated robust catalytic performance in removing SDZ (96.15%), RhB (93.02%) and phenol (57.03%) within 360 min (Fig. 8c). When a voltage of 0.4 V was applied, the degrade rate constant (k<sub>obs</sub>) was further increased by 1.6 – 2.5 times. Although this enhancement in actual sunlight was similar to that under LED light irradiation (2.43 times), the overall performance of TiO<sub>2</sub> NNs-NCDs/Co<sub>3</sub>O<sub>4</sub> PEC system decreased. This could be due to the slow change in the irradiation direction of the sunlight during the PEC process, resulting in insufficient utilization of sunlight by the photoelectrode. Regardless of the decreased activity, the removal efficiency of these pollutants by this dual-photoelectrode PEC system could reach more than 94% under the real sunlight irradiation. Besides, TiO<sub>2</sub> NNs-NCDs/Co<sub>3</sub>O<sub>4</sub> was the only PEC system reported so far that could use actual sunlight to degrade pollutants with low or no electrical energy input as far as we know (Table S6). And, TiO<sub>2</sub> NNs-NCDs/Co<sub>3</sub>O<sub>4</sub> system had higher degradation activity and stability compared to other dual-photoelectrode PEC systems. The above results demonstrated that the TiO<sub>2</sub> NNs-NCDs/Co<sub>3</sub>O<sub>4</sub> is a promising PEC cell with fascinating properties for water purification.

## 4. Conclusions

Overall, we presented an efficient and energy-saving TiO<sub>2</sub> NNs-NCDs/Co<sub>3</sub>O<sub>4</sub> PEC system that can be operated at low or even without external voltage. At the low cell voltage of 0.4 V (anodic potential = 0.1 V vs. Ag/AgCl), the k<sub>obs</sub> of SDZ degradation by TiO<sub>2</sub> NNs-NCDs/Co<sub>3</sub>O<sub>4</sub> system was 0.0538 min<sup>-1</sup>, which was about 6.64 and 16.30 times higher than TiO<sub>2</sub> NNs-Pt (0.0081 min<sup>-1</sup>) and Pt-NCDs/Co<sub>3</sub>O<sub>4</sub> (0.0033 min<sup>-1</sup>), respectively. The improved catalytic performance could be attributed to the strong internal photovoltage (0.389 V) generated by the potential difference of quasi-Femi energy between the TiO<sub>2</sub> NNs/Ti mesh photoanode and NCDs/Co<sub>3</sub>O<sub>4</sub>/Ti mesh photocathode. Quenching experiments and probe tests, as well as EPR analysis, clearly revealed that the dominant ROS for SDZ decomposition in the dual-photoelectrode PEC system followed the order: •OH > e<sup>-</sup> > •O<sub>2</sub><sup>-</sup>. Satisfactorily, the TiO<sub>2</sub> NNs-NCDs/Co<sub>3</sub>O<sub>4</sub> PEC system possessed outstanding performance in real water matrices (e.g., 97.66% of SDZ in lake water), reusability (97.40% and 0.0527 min<sup>-1</sup> of 20 cycles), leaching resistance of cobalt ions (0.020 mg L<sup>-1</sup>) and low energy consumption (E<sub>EO</sub> = 2.09 kWh m<sup>-3</sup> order<sup>-1</sup>). Moreover, this novel dual-photoelectrode PEC system had the potential for practical applications, which could use the real sunlight to eliminate pollutants under no external voltage (e.g., SDZ, 95.91%, 300 min), or at a low cell voltage of 0.4 V (e.g., SDZ, 98.16%, 180 min). This work provides novel inspirations for the development of a sustainable, energy-saving, and strong-stable PEC system for wastewater treatment.

## CRediT authorship contribution statement

Zhongzheng Hu: Conceptualization, Methodology, Formal analysis,

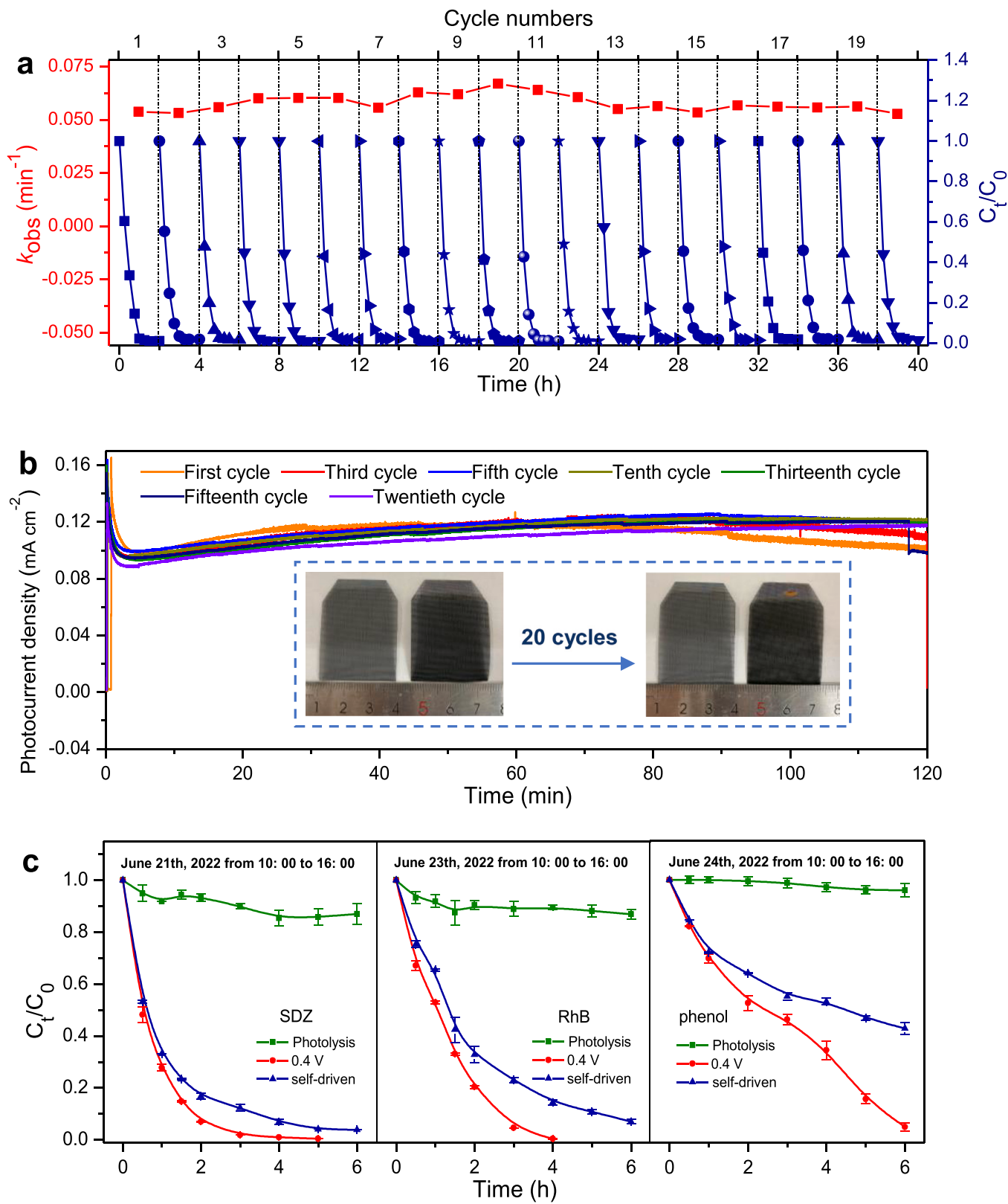


**Fig. 8.** (a) Recycling runs for SDZ removal in TiO<sub>2</sub> NNS-NCDs/Co<sub>3</sub>O<sub>4</sub> system. (b)  $J-t$  plots during SDZ degradation in cycle tests with the inset of the digital images of TiO<sub>2</sub> NNS/Ti mesh and NCDs/Co<sub>3</sub>O<sub>4</sub>/Ti mesh before and after 20 cycle tests. (c) PEC performance for wastewater treatment of TiO<sub>2</sub> NNS-NCDs/Co<sub>3</sub>O<sub>4</sub> system under illumination with real sunlight from 10:00-16:00 (Tianjin, China).

Investigation, Data curation, Writing – original draft, Writing – review & editing. **Minghua Zhou**: Conceptualization, Supervision, Funding acquisition, Resources, Writing – review & editing. **Hubdar Ali Maitlo**: Writing – review & editing, Data curation. **Ruiheng Liang**: Writing – review & editing, Data curation. **Yang Zheng**: Validation, Visualization. **Huizhong Wu**: Validation, Visualization. **XiangRu Song**: Writing – review & editing. **Omotayo A. Arotibac**: Writing – review & editing.

## Declaration of Competing Interest

The authors declare that they have no known competing financial interests or personal relationships that could have appeared to influence the work reported in this paper.

## Data Availability

Data will be made available on request.

## Acknowledgements

This work was financially supported by National Key Research and Development Program International Cooperation Project (2021YFE0106500), Key Project of Natural Science Foundation of Tianjin (no. 21JCZDJC00320), Natural Science Foundation of China (nos. 52170085 and 21976096), Fundamental Research Funds for the Central Universities, Nankai University, and National Research Foundation IRG - China/South Africa Research Cooperation Programme (Grant Number 132793).

## Appendix A. Supporting information

Supplementary data associated with this article can be found in the online version at [doi:10.1016/j.apcatb.2023.122676](https://doi.org/10.1016/j.apcatb.2023.122676).

## References

- [1] Y. Deng, B. Li, K. Yu, T. Zhang, Biotransformation and adsorption of pharmaceutical and personal care products by activated sludge after correcting matrix effects, *Sci. Total. Environ.* 544 (2016) 980–986, <https://doi.org/10.1016/j.scitotenv.2015.12.010>.
- [2] S. Kumar, C. Tewari, N.G. Sahoo, L. Philip, Mechanistic insights into carbocatalyzed persulfate treatment for simultaneous degradation of cationic and anionic dye in multicomponent mixture using plastic waste-derived carbon, *J. Hazard. Mater.* 435 (2022) 128956, <https://doi.org/10.1016/j.jhazmat.2022.128956>.
- [3] A.S. Oberoi, Y. Jia, H. Zhang, S.K. Khanal, H. Lu, Insights into the fate and removal of antibiotics in engineered biological treatment systems: a critical review, *Environ. Sci. Technol.* 53 (2019) 7234–7264, <https://doi.org/10.1021/acs.est.9b01131>.
- [4] L.T. Qin, X.R. Pang, H.H. Zeng, Y.P. Liang, L.Y. Mo, D.Q. Wang, J.F. Dai, Ecological and human health risk of sulfonamides in surface water and groundwater of Huixian karst wetland in Guilin, China, *Sci. Total. Environ.* 708 (2020) 134552, <https://doi.org/10.1016/j.scitotenv.2019.134552>.
- [5] P. Xie, C. Chen, C. Zhang, G. Su, N. Ren, S.H. Ho, Revealing the role of adsorption in ciprofloxacin and sulfadiazine elimination routes in microalgae, *Water Res.* 172 (2020) 115475, <https://doi.org/10.1016/j.watres.2020.115475>.
- [6] M.S.P. Yadav, N. Neghi, M. Kumar, G.K. Varghese, Photocatalytic-oxidation and photo-persulfate-oxidation of sulfadiazine in a laboratory-scale reactor: Analysis of catalyst support, oxidant dosage, removal-rate and degradation pathway, *J. Environ. Manag.* 222 (2018) 164–173, <https://doi.org/10.1016/j.jenvman.2018.05.052>.
- [7] Z. Hu, X. Xie, S. Li, M. Song, G. Liang, J. Zhao, Z. Wang, Rational construct CQDs/BiOCOOH/uCN photocatalyst with excellent photocatalytic performance for degradation of sulfathiazole, *Chem. Eng. J.* 404 (2021) 126541, <https://doi.org/10.1016/j.cej.2020.126541>.
- [8] Sustainable water solutions, *Nat. Sustain.* 3 (2020) 73–73. <https://doi.org/10.1038/s41893-020-0481-1>.
- [9] C. Jiang, S.J.A. Moniz, A. Wang, T. Zhang, J. Tang, Photoelectrochemical devices for solar water splitting - materials and challenges, *Chem. Soc. Rev.* 46 (2017) 4645–4660, <https://doi.org/10.1039/c6cs00306k>.
- [10] Y. Zhao, C. Deng, D. Tang, L. Ding, Y. Zhang, H. Sheng, H. Ji, W. Song, W. Ma, C. Chen, J. Zhao,  $\alpha$ -Fe<sub>2</sub>O<sub>3</sub> as a versatile and efficient oxygen atom transfer catalyst in combination with H<sub>2</sub>O<sub>2</sub> as the oxygen source, *Nat. Catal.* 4 (2021) 684–691, <https://doi.org/10.1038/s41929-021-00659-1>.
- [11] R. Song, H. Chi, Q. Ma, D. Li, X. Wang, W. Gao, H. Wang, X. Wang, Z. Li, C. Li, Highly efficient degradation of persistent pollutants with 3D nanocone TiO<sub>2</sub>-based photoelectrocatalysis, *J. Am. Chem. Soc.* 143 (2021) 13664–13674, <https://doi.org/10.1021/jacs.1c05008>.
- [12] Y. Feng, H.H.M. Rijnaarts, D. Yntema, Z. Gong, D.D. Dionysiou, Z. Cao, S. Miao, Y. Chen, Y. Ye, Y. Wang, Applications of anodized TiO<sub>2</sub> nanotube arrays on the removal of aqueous contaminants of emerging concern: a review, *Water Res.* 186 (2020) 116327, <https://doi.org/10.1016/j.watres.2020.116327>.
- [13] Q. Ma, R. Song, F. Ren, H. Wang, W. Gao, Z. Li, C. Li, Photoelectrocatalytic degradation of refractory pollutants over WO<sub>3</sub>/W network photoelectrode with heterophase junction for enhancing mass transportation and charge separation, *Appl. Catal. B-Environ.* 309 (2022) 121292, <https://doi.org/10.1016/j.apcatb.2022.121292>.
- [14] J. Wang, Z. Yang, X. Gao, W. Yao, W. Wei, X. Chen, R. Zong, Y. Zhu, Core-shell g-C<sub>3</sub>N<sub>4</sub>@ZnO composites as photoanodes with double synergistic effects for enhanced visible-light photoelectrocatalytic activities, *Appl. Catal. B-Environ.* 217 (2017) 169–180, <https://doi.org/10.1016/j.apcatb.2017.05.034>.
- [15] P. Mazierski, A.F. Borzyszkowska, P. Wilczewska, A. Bialk-Bielinska, A. Zaleska-Medynska, E.M. Siedlecka, A. Pieczynska, Removal of 5-fluorouracil by solar-driven photoelectrocatalytic oxidation using Ti/TiO<sub>2</sub>(NT) photoelectrodes, *Water Res.* 157 (2019) 610–620, <https://doi.org/10.1016/j.watres.2019.04.010>.
- [16] J. Zhang, G. Zhang, H. Lan, J. Qu, H. Liu, Synergetic hydroxyl radical oxidation with atomic hydrogen reduction lowers the organochlorine conversion barrier and potentiates effective contaminant mineralization, *Environ. Sci. Technol.* 55 (2021) 3296–3304, <https://doi.org/10.1021/acs.est.0c07271>.
- [17] S. Chen, L.-W. Wang, Thermodynamic oxidation and reduction potentials of photocatalytic semiconductors in aqueous solution, *Chem. Mater.* 24 (2012) 3659–3666, <https://doi.org/10.1021/cm302533s>.
- [18] J. Zheng, H. Zhou, Y. Zou, R. Wang, Y. Lyu, S.P. Jiang, S. Wang, Efficiency and stability of narrow-gap semiconductor-based photoelectrodes, *Energy Environ. Sci.* 12 (2019) 2345–2374, <https://doi.org/10.1039/c9ee00524b>.
- [19] C.Y. Toe, J. Scott, R. Amal, Y.H. Ng, Recent advances in suppressing the photocorrosion of cuprous oxide for photocatalytic and photoelectrochemical energy conversion, *J. Photoch. Photobiol. C* 40 (2019) 191–211, <https://doi.org/10.1016/j.jphotochemrev.2018.10.001>.
- [20] Y. He, K. Chen, M.K.H. Leung, Y. Zhang, L. Li, G. Li, J. Xuan, J. Li, Photocatalytic fuel cell – a review, *Chem. Eng. J.* 428 (2022) 131074, <https://doi.org/10.1016/j.cej.2021.131074>.
- [21] Q. Chen, J. Li, X. Li, K. Huang, B. Zhou, W. Cai, W. Shangguan, Visible-light responsive photocatalytic fuel cell based on WO<sub>3</sub>/W photoanode and Cu<sub>2</sub>O/Cu photocathode for simultaneous wastewater treatment and electricity generation, *Environ. Sci. Technol.* 46 (2012) 11451–11458, <https://doi.org/10.1021/es302651q>.
- [22] W. Yang, R.R. Prabhakar, J. Tan, S.D. Tilley, J. Moon, Strategies for enhancing the photocurrent, photovoltage, and stability of photoelectrodes for photoelectrochemical water splitting, *Chem. Soc. Rev.* 48 (2019) 4979–5015, <https://doi.org/10.1039/c8cs00997j>.
- [23] T. Zhou, S. Chen, L. Li, J. Wang, Y. Zhang, J. Li, J. Bai, L. Xia, Q. Xu, M. Rahim, B. Zhou, Carbon quantum dots modified anatase/rutile TiO<sub>2</sub> photoanode with dramatically enhanced photoelectrochemical performance, *Appl. Catal. B-Environ.* 269 (2020) 118776, <https://doi.org/10.1016/j.apcatb.2020.118776>.
- [24] Y. Hou, F. Zuo, A. Dagg, P. Feng, A three-dimensional branched cobalt-doped  $\alpha$ -Fe<sub>2</sub>O<sub>3</sub> nanorod/MgFe<sub>2</sub>O<sub>4</sub> heterojunction array as a flexible photoanode for efficient photoelectrochemical water oxidation, *Angew. Chem. Int. Ed.* 52 (2013) 1248–1252, <https://doi.org/10.1002/anie.201207578>.
- [25] J. Wu, X. Han, D. Li, B.E. Logan, J. Liu, Z. Zhang, Y. Feng, Efficient CO<sub>2</sub> conversion to formic acid in a novel microbial photoelectrochemical cell using a visible-light responsive Co<sub>3</sub>O<sub>4</sub> nanorod-arrayed photocathode, *Appl. Catal. B-Environ.* 276 (2020) 119102, <https://doi.org/10.1016/j.apcatb.2020.119102>.
- [26] J. Gao, B. Jiang, C. Ni, Y. Qi, Y. Zhang, N. Oturan, M.A. Oturan, Non-precious Co<sub>3</sub>O<sub>4</sub>/TiO<sub>2</sub>/Ti cathode based electrocatalytic nitrate reduction: Preparation, performance and mechanism, *Appl. Catal. B-Environ.* 254 (2019) 391–402, <https://doi.org/10.1016/j.apcatb.2019.05.016>.
- [27] F. Zhao, W. Li, Y. Song, Y. Fu, X. Liu, C. Ma, G. Ma, X. Dong, H. Ma, Constructing S-scheme Co<sub>3</sub>O<sub>4</sub>-C<sub>6</sub>N<sub>4</sub> catalyst with superior photoelectrocatalytic efficiency for water purification, *Appl. Mater. Today* 26 (2022) 101390, <https://doi.org/10.1016/j.apmt.2022.101390>.
- [28] J. Wu, Y. Han, Y. Bai, X. Wang, Y. Zhou, W. Zhu, T. He, Y. Wang, H. Huang, Y. Liu, Z. Kang, The electron transport regulation in carbon Dots/In<sub>2</sub>O<sub>3</sub> electrocatalyst enable 100% selectivity for oxygen reduction to hydrogen peroxide, *Adv. Funct. Mater.* 32 (2022) 2203647, <https://doi.org/10.1002/adfm.202203647>.
- [29] Q. Wu, J. Cao, X. Wang, Y. Liu, Y. Zhao, H. Wang, Y. Liu, H. Huang, F. Liao, M. Shao, Z. Kang, A metal-free photocatalyst for highly efficient hydrogen peroxide photoproduction in real seawater, *Nat. Commun.* 12 (2021) 483, <https://doi.org/10.1038/s41467-020-20823-8>.
- [30] D. Pan, S. Xiao, X. Chen, R. Li, Y. Cao, D. Zhang, S. Pu, Z. Li, G. Li, H. Li, Efficient photocatalytic fuel cell via simultaneous visible-photoelectrocatalytic degradation and electricity generation on a porous coral-like WO<sub>3</sub>/W photoelectrode, *Environ. Sci. Technol.* 53 (2019) 3697–3706, <https://doi.org/10.1021/acs.est.8b05685>.
- [31] P. Su, M. Zhou, X. Lu, W. Yang, G. Ren, J. Cai, Electrochemical catalytic mechanism of N-doped graphene for enhanced H<sub>2</sub>O<sub>2</sub> yield and in-situ degradation of organic pollutant, *Appl. Catal. B-Environ.* 245 (2019) 583–595, <https://doi.org/10.1016/j.apcatb.2018.12.075>.
- [32] G. Kresse, J. Furthmüller, Efficiency of ab-initio total energy calculations for metals and semiconductors using a plane-wave basis set, *Comp. Mater. Sci.* 6 (1996) 15–50, [https://doi.org/10.1016/0927-0256\(96\)00008-0](https://doi.org/10.1016/0927-0256(96)00008-0).

[33] G. Kresse, J. Furthmüller, Efficient iterative schemes for ab initio total-energy calculations using a plane-wave basis set, *Phys. Rev. B* 54 (1996) 11169–11186, <https://doi.org/10.1103/PhysRevB.54.11169>.

[34] J.P. Perdew, K. Burke, M. Ernzerhof, Generalized gradient approximation made simple, *Phys. Rev. Lett.* 77 (1996) 3865–3868, <https://doi.org/10.1103/PhysRevLett.77.3865>.

[35] D. Zhong, B. Cai, X. Wang, Z. Yang, Y. Xing, S. Miao, W.-H. Zhang, C. Li, Synthesis of oriented  $TiO_2$  nancones with fast charge transfer for perovskite solar cells, *Nano Energy* 11 (2015) 409–418, <https://doi.org/10.1016/j.nanoen.2014.11.014>.

[36] M. Yu, Z. Wang, C. Hou, Z. Wang, C. Liang, C. Zhao, Y. Tong, X. Lu, S. Yang, Nitrogen-doped  $Co_3O_4$  mesoporous nanowire arrays as an additive-free air-cathode for flexible solid-state zinc-air batteries, *Adv. Mater.* 29 (2017) 1602868, <https://doi.org/10.1002/adma.201602868>.

[37] X. Miao, X. Yue, Z. Ji, X. Shen, H. Zhou, M. Liu, K. Xu, J. Zhu, G. Zhu, L. Kong, S. A. Shah, Nitrogen-doped carbon dots decorated on  $g-C_3N_4/Ag_3PO_4$  photocatalyst with improved visible light photocatalytic activity and mechanism insight, *Appl. Catal. B-Environ.* 227 (2018) 459–469, <https://doi.org/10.1016/j.apcatb.2018.01.057>.

[38] M. Song, Z. Zhang, Q. Li, W. Jin, Z. Wu, G. Fu, X. Liu, Ni-foam supported  $Co(OH)F$  and Co-P nanoarrays for energy-efficient hydrogen production via urea electrolysis, *J. Mater. Chem. A* 7 (2019) 3697–3703, <https://doi.org/10.1039/c8ta10985k>.

[39] X. Zhang, J. Xiao, X. Zhang, Y. Meng, D. Xiao, Three-dimensional  $Co_3O_4$  nanowires@amorphous  $Ni(OH)_2$  ultrathin nanosheets hierarchical structure for electrochemical energy storage, *Electrochim. Acta* 191 (2016) 758–766, <https://doi.org/10.1016/j.electacta.2016.01.159>.

[40] Z. Gu, X. An, H. Lan, Y. Tian, J. Zhang, R. Liu, H. Liu, J. Qu, Microfluidic-enhanced 3-D photoanodes with free interfacial energy barrier for photoelectrochemical applications, *Appl. Catal. B-Environ.* 244 (2019) 740–747, <https://doi.org/10.1016/j.apcatb.2018.12.009>.

[41] M.G. Lee, J.W. Yang, H. Park, C.W. Moon, D.M. Andoshe, J. Park, C.K. Moon, T. H. Lee, K.S. Choi, W.S. Cheon, J.J. Kim, H.W. Jang, Crystal facet engineering of  $TiO_2$  nanostructures for enhancing photoelectrochemical water splitting with  $BiVO_4$  nanodots, *Nanomicro Lett.* 14 (2022) 48, <https://doi.org/10.1007/s40820-022-00795-8>.

[42] F. Liu, R. Shi, Z. Wang, Y. Weng, C.M. Che, Y. Chen, Direct Z-scheme hetero-phase junction of black/red phosphorus for photocatalytic water splitting, *Angew. Chem. Int. Ed.* 58 (2019) 11791–11795, <https://doi.org/10.1002/anie.201906416>.

[43] J.B.L.G. Xia, J.H. Li, Q.Y. Zeng, X.J. Li, B.X. Zhou, A highly efficient  $BiVO_4/WO_3/W$  heterojunction photoanode for visible-light responsive dual photoelectrode photocatalytic fuel cell, *Appl. Catal. B-Environ.* 183 (2016) 224–230, <https://doi.org/10.1016/j.apcatb.2015.10.050>.

[44] Y. Hu, Q. Niu, Y. Wang, Y.-n Zhang, G. Zhao, Highly efficient removal mechanism of dimethyl phthalate over an economical 3D {001}  $TiO_2/Ti$  photoelectrode with enhanced photoelectrocatalytic activity and long service life, *Appl. Catal. B-Environ.* 285 (2021) 119812, <https://doi.org/10.1016/j.apcatb.2020.119812>.

[45] K. Qi, Y. Ye, B. Wei, M. Li, Y. Lun, X. Xie, H. Xie, N-QDs from reed straw enriching charge over  $BiO_{2-x}/BiOCl$  p-n heterojunction for improved visible-light-driven photodegradation of organic pollutants, *J. Hazard. Mater.* 432 (2022) 128759, <https://doi.org/10.1016/j.jhazmat.2022.128759>.

[46] Z. Gu, J. Zhou, X. An, Q. Chen, C. Hu, H. Liu, J. Qu, A dual-biomimetic photocatalytic fuel cell for efficient electricity generation from degradation of refractory organic pollutants, *Appl. Catal. B-Environ.* 298 (2021) 120501, <https://doi.org/10.1016/j.apcatb.2021.120501>.

[47] Z. Zheng, I.M.C. Lo, Fabrication of  $MoS_2@BL-BiVO_4$  photoanode with promoted charge separation for photoelectrochemical sewage treatment to simultaneously degrade PPCPs, disinfect *E. coli*, and produce  $H_2$ : performance, mechanisms, and influence factors, *Appl. Catal. B-Environ.* 299 (2021) 120636, <https://doi.org/10.1016/j.apcatb.2021.120636>.

[48] K.H. Ye, H. Li, D. Huang, S. Xiao, W. Qiu, M. Li, Y. Hu, W. Mai, H. Ji, S. Yang, Enhancing photoelectrochemical water splitting by combining work function tuning and heterojunction engineering, *Nat. Commun.* 10 (2019) 3687, <https://doi.org/10.1038/s41467-019-11586-y>.

[49] J.H. Kim, J.S. Lee, Elaborately modified  $BiVO_4$  photoanodes for solar water splitting, *Adv. Mater.* 31 (2019) 1806938, <https://doi.org/10.1002/adma.201806938>.

[50] A. Kumar, M. Khan, J. He, I.M.C. Lo, Recent developments and challenges in practical application of visible-light-driven  $TiO_2$ -based heterojunctions for PPCP degradation: a critical review, *Water Res.* 170 (2020) 115356, <https://doi.org/10.1016/j.watres.2019.115356>.

[51] J. Wang, S. Wang, Effect of inorganic anions on the performance of advanced oxidation processes for degradation of organic contaminants, *Chem. Eng. J.* 411 (2021) 128392, <https://doi.org/10.1016/j.cej.2020.128392>.

[52] G. Wang, Q. Chen, Y. Liu, D. Ma, Y. Xin, X. Ma, X. Zhang, In situ synthesis of graphene/ $WO_3$  co-decorated  $TiO_2$  nanotube array photoelectrodes with enhanced photocatalytic activity and degradation mechanism for dimethyl phthalate, *Chem. Eng. J.* 337 (2018) 322–332, <https://doi.org/10.1016/j.cej.2017.12.058>.

[53] Y. Feng, Q. Song, W. Lv, G. Liu, Degradation of ketoprofen by sulfate radical-based advanced oxidation processes: Kinetics, mechanisms, and effects of natural water matrices, *Chemosphere* 189 (2017) 643–651, <https://doi.org/10.1016/j.chemosphere.2017.09.109>.

[54] M.S. Koo, X. Chen, K. Cho, T. An, W. Choi, In Situ photoelectrochemical chloride activation using a  $WO_3$  electrode for oxidative treatment with simultaneous  $H_2$  evolution under visible light, *Environ. Sci. Technol.* 53 (2019) 9926–9936, <https://doi.org/10.1021/acs.est.9b02401>.

[55] X. Yang, F.L. Rosario-Ortiz, Y. Lei, Y. Pan, X. Lei, P. Westerhoff, Multiple roles of dissolved organic matter in advanced oxidation processes, *Environ. Sci. Technol.* 56 (2022) 11111–11131, <https://doi.org/10.1021/acs.est.2c01017>.

[56] Z.H. Xie, C.S. He, H.Y. Zhou, L.L. Li, Y. Liu, Y. Du, W. Liu, Y. Mu, B. Lai, Effects of molecular structure on organic contaminants' degradation efficiency and dominant ROS in the advanced oxidation process with multiple ROS, *Environ. Sci. Technol.* 56 (2022) 8784–8795, <https://doi.org/10.1021/acs.est.2c00464>.

[57] L. Wang, B. Li, D.D. Dionysiou, B. Chen, J. Yang, J. Li, Overlooked formation of  $H_2O_2$  during the hydroxyl radical-scavenging process when using alcohols as scavengers, *Environ. Sci. Technol.* 56 (2022) 3386–3396, <https://doi.org/10.1021/acs.est.1c03796>.

[58] L.S. Zhang, X.H. Jiang, Z.A. Zhong, L. Tian, Q. Sun, Y.T. Cui, X. Lu, J.P. Zou, S. L. Luo, Carbon nitride supported high-loading Fe single-atom catalyst for activation of peroxymonosulfate to generate  $^1O_2$  with 100% selectivity, *Angew. Chem. Int. Ed.* 60 (2021) 21751–21755, <https://doi.org/10.1002/anie.202109488>.

[59] Y. Nosaka, A.Y. Nosaka, Generation and detection of reactive oxygen species in photocatalysis, *Chem. Rev.* 117 (2017) 11302–11336, <https://doi.org/10.1021/acs.chemrev.7b00161>.

[60] A. Ansari, D. Nematollahi, Convergent paired electrocatalytic degradation of p-dinitrobenzene by  $Ti/SnO_2-Sb/\beta-PbO_2$  anode. A new insight into the electrochemical degradation mechanism, *Appl. Catal. B-Environ.* 261 (2020) 118226, <https://doi.org/10.1016/j.apcatb.2019.118226>.